

CZECH TECHNICAL UNIVERSITY IN PRAGUE
FACULTY OF NUCLEAR SCIENCE AND PHYSICAL ENGINEERING

Department of Physics

Physics and Technology of Nuclear Fusion



BACHELOR'S THESIS

**Detection of Fast Ions from Laser-Generated
Plasma**

Detekce Rychlých Iontů z Laserového Plazmatu

Author: Valeriia Istokskaja
Supervisor: Lorenzo Giuffrida, Ph.D.
Consultant: Ing. Jan Pšikal, Ph.D.
Prague, 2017



Katedra: fyziky

Akademický rok: 2016/2017

ZADÁNÍ BAKALÁŘSKÉ PRÁCE

Student: Valeria Istoksaia

Studijní program: Aplikace přírodních věd

Obor: Fyzika a technika termojaderné fúze

Název práce: Detekce rychlých iontů z laserového plazmatu
(česky)

Název práce: Detection of fast ions from laser-generated plasma
(anglicky)

Pokyny pro vypracování:

- 1) Stručné shrnutí teorie generování/urychlování iontů při interakci laserového záření s plazmatem
- 2) Diagnostika rychlých iontů vznikajících při interakci laserového záření s plazmatem pomocí metody doby průletu (time-of-flight)
- 3) Analýza experimentálních dat naměřených time-of-flight detektorem včetně vysvětlení metod použitých pro tuto analýzu

Doporučená literatura:

- [1] A. Macchi et al.: Ion acceleration by superintense laser-plasma interaction, Rev. Mod. Phys. 85, 751 (2013).
- [2] H. Daido et al., Review of laser-driven ion sources and their applications, Rep. Prog. Phys. 75, 056401 (2012).
- [3] D. Margarone et al., Full characterization of laser-accelerated ion beams using Faraday cup, silicon carbide, and single-crystal diamond detectors, J. Appl. Phys. 109, 103302 (2011).
- [4] J. Krasa, Gaussian energy distribution of fast ions emitted by laser-produced plasmas, Appl. Surf. Sci. 272, 46 (2013).

Jméno a pracoviště vedoucího bakalářské práce:

Dr. Lorenzo Giuffrida, Fyzikální ústav, AV ČR, v.v.i., Praha

Jméno a pracoviště konzultanta:

Ing. Jan Pšikal, Ph.D., Katedra fyzikální elektroniky, Fakulta jaderná a fyzikálně inženýrská, ČVUT v Praze

Datum zadání bakalářské práce: 20.10.2016

Termín odevzdání bakalářské práce: 10.07.2017

Doba platnosti zadání je dva roky od data zadání.


.....
vedoucí katedry




.....
děkan

V Praze dne 20.10.2016

Prohlášení

Prohlašuji, že jsem svou bakalářskou práci vypracovala samostatně a použila jsem pouze podklady (literaturu, projekty, SW atd.) uvedené v příloženém seznamu.

Nemám závažný důvod proti použití tohoto školního díla ve smyslu §60 Zákona č. 121/2000 Sb., o právu autorském, o právech souvisejících s právem autorským a o změně některých zákonů (autorský zákon).

V Praze dne

.....
Valeriia Istoksaia

Acknowledgement

I would like to express my sincere gratitude to my supervisor Lorenzo Giuffrida, Ph.D. for his guidance, patience and encouragement throughout the learning process of this bachelor thesis.

Furthemore, I would like to thank my consultant Ing. Jan Pšikal, Ph.D. for providing me with expert advices and useful suggestions, especially about the theoretical part of the thesis.

Valeriia Istokskaia

Název práce: **Detekce Rychlých Iontů z Laserového Plazmatu**

Autor: Valeriia Istokskaia

Obor: Fyzika a Technika Termojaderné Fúze

Druh práce: Bakalářská práce

Vedoucí práce: Lorenzo Giuffrida, Ph.D., FZÚ AV ČR

Konzultant: Ing. Jan Pšikal, Ph.D., KFE FJFI ČVUT

Abstrakt: Laserem urychlené iontové svazky mohou být potenciálně využity v multidisciplinárních oblastech, např. v jaderné fyzice, vědě o materiálech nebo při protonové terapii. Pro tyto účely musí být svazky dobře charakterizovány. První část této práce shrnuje základní teoretické myšlenky týkající se fyziky laserového plazmatu, včetně popisu mechanismů absorpce laserového záření v plazmatu a nejznámějších mechanismů urychlování nabitých částic. Práce pokračuje popisem nejpoužívanějších detektorů urychlených iontů. Práce je především zaměřená na analýzu výsledků vybraných měření v experimentech pomocí detektorů založených na metodě doby průletu (time-of-flight). V poslední kapitole je uvedena analýza dat, naměřených během dvou různých experimentů, jeden z nichž proběhl v laserovém centru v Lundu (LLC) ve Švédsku a druhý v badatelském centru PALS v Praze v roce 2016. Popis těchto experimentů je taky uveden v této kapitole.

Klíčová slova: diagnostika iontových svazků, urychlování laserem, fyzika plazmatu, měření doby průletu (TOF)

Title of work: **Detection of Fast Ions from Laser-Generated Plasma**

Author: Valeriia Istokskaia

Specialization: Physics and Technology of Nuclear Fusion

Type of thesis: Bachelor thesis

Supervisor: Lorenzo Giuffrida, Ph.D., FZÚ AV ČR

Consultant: Ing. Jan Pšikal, Ph.D., KFE FJFI ČVUT

Abstract: Laser-accelerated ion beams can be potentially applied in multidisciplinary fields, e.g. in nuclear Physics, material science and hadrontherapy. For these purposes beams have to be properly characterized. The first part of the thesis summaries basic theoretical concepts concerning laser plasma physics, including the description of laser absorption and some of the most well-known and studied acceleration mechanisms. This is followed by the description of the most commonly used ion detectors. The thesis is focused mainly on the on the analysis of some measurements performed by using detectors working in time-of-flight configuration. The last part of the thesis contains the analysis of data acquired in two different experiments, performed at the Lund Laser Center (LLC) in Sweden and at the Prague Asterix Laser System (PALS) in Prague in 2016. The description of these experiments is introduced as well.

Key words: ion beam diagnostics, laser acceleration, plasma physics, Time of flight (TOF) technique

Contents

Introduction	1
1 Theory of laser-plasma interaction and particle acceleration	3
1.1 Basic characteristics of plasma	3
1.1.1 Debye shielding	3
1.1.2 Plasma frequency	4
1.2 Propagation of laser wave in plasma	5
1.3 Absorption of laser radiation in plasma	6
1.3.1 Resonant Absorption	7
1.3.2 Vacuum Heating	7
1.3.3 Relativistic $\mathbf{j} \times \mathbf{b}$ Heating	8
1.4 Mechanisms of laser-driven acceleration of ions	8
1.4.1 Target Normal Sheath Acceleration (TNSA)	9
1.4.2 Radiation Pressure Acceleration (RPA)	11
2 Detection of accelerated ions from plasma	13
2.1 Time-of-flight detectors	13
2.1.1 Ion collector	15
2.1.2 Semiconductor detectors	16
2.1.3 SiC detector	16
2.1.4 Diamond detector	18
2.2 Thomson parabola	20
2.3 Radiochromic films	22
3 Experiments and data analysis	24
3.1 Technique of deconvolution	24
3.2 Experiment at Lund Laser Center	26
3.2.1 Experimental setup	27
3.3 Data analysis	28
3.3.1 Shot 9: Mylar target	28
3.3.2 Shot 12: Mylar + Nanosphere target	30
3.3.3 Comparisons of shots and of obtained and published results	33
3.4 Experiment at Prague Asterix Laser System	33
Conclusion	38

Introduction

Plasma is considered as the “fourth state” of matter that can emerge from the heated or photo-ionized gas, similarly to how gases can derive from liquid by increasing the temperature. Almost 99% of matter in the universe is in the state of plasma – all stars, galactic nebulae and interstellar medium are examples of this ionized state. However, plasma is a very rare natural phenomenon on the Earth, and it is hard to generate it artificially from neutral gases because of high temperatures required. Apparently from the gas, plasma is composed of positive and negative charged particles (and neutrals), experiencing collective motions. Under normal conditions plasma ions and electrons are in equilibrium, but if a strong external electromagnetic (or electric) field is applied on plasma, it can perturb the latter and induce a charge separation field that, in its turn, can accelerate ions in very short distances.

With the progress in laser technology in the last decades, it became possible to use lasers for plasma production and subsequently for plasma acceleration. Nowadays, ions with the energy of several tens of MeV can be accelerated by using a laser with high intensity and short pulse duration [1]. The science field, that deals with the laser-plasma interaction, is called Laser Plasma Physics. Besides particle acceleration, it is applicable also in nuclear fusion, astrophysics, material science and medicine.

Presently, new generation of large facility with the aim to study the interaction of an ultraintense laser (at PW level) with a target are under construction, for example Extreme Light Infrastructure (ELI) in Prague. This facility will possess lasers with ultra-high peak powers and focused intensities, that will enable deeper research in all fields of laser plasma physics application. In the case of particle acceleration, the improvement of particle beam parameters, such as maximum energy and number of accelerated particles are anticipated. However, these beam parameters can be difficult to be measured. To characterize such laser-accelerated particle beams as precise as possible, appropriate diagnostics is needed. This thesis is dedicated to the demonstration of advantages of using detectors working in time-of-flight (TOF) technique, especially semiconductor detectors, when characterizing the beam in terms of ion species, maximum energy and number of particles. Precise values of these parameters are very important for the application of laser-accelerated beams in radiotherapy (hadrontherapy). Among other issues, semiconductor detectors solve the problem of the presence of wide photopeak, induced by XUV radiation, on recorded spectra, that prevents high energetic particles (hence the maximum energy) from being detected.

The first chapter of the thesis summarizes the theory of laser-plasma interaction and particle acceleration mechanisms. Basic characteristics of plasma are described at the beginning, followed by mechanisms of laser absorption, such as resonant absorption, vacuum and relativistic $\vec{j} \times \vec{B}$ heating. Finally, acceleration mechanisms are described,

namely Target normal sheath acceleration (TNSA) and Radiation pressure acceleration (RPA).

Second chapter aims to give an overview of some of the most common ion detection techniques used nowadays. Chapter is focused on TOF detectors, introducing Faraday cup and semiconductor detectors, such as Silicon carbide (SiC) and Diamond detector (DD). Also, the Thomson parabola spectrometer and Radiochromic films are described there.

Chapter 3 contains the analysis of data acquired using SiC or DD detectors during two experiments, performed in 2016, aimed to accelerate ions during the laser-to-target interaction. The description of deconvolution technique, applied to interpret the data, is presented here as well.

Chapter 1

Theory of laser-plasma interaction and particle acceleration

1.1 Basic characteristics of plasma

Plasma is a quasineutral gas of charged and neutral particles which exhibits collective behavior [2]. Namely this means that motions depend not only on local conditions but also on the state of the plasma in distant regions. Quasineutrality means that at the large scales, a plasma appears electrically neutral, as charge fluctuations in plasma are compensated at the dimensions much larger than a Debye length distance. This is the result of a phenomenon called Debye shielding. Also, the plasma appears quasineutral at time scale much larger than the reciprocal plasma frequency.

1.1.1 Debye shielding

A fundamental property of a plasma is the ability to shield (screen) intrinsic electric potentials. The shielding is implemented by the slight displacement of charged plasma particles so as to reduce the effectiveness of the arisen field. If some "test" particle carrying non-zero charge is placed into the initially unperturbed plasma, it starts to attract opposite charges. Thus, a cloud of charged particles surrounding primal particle emerges. In the case of cold plasma, where particles have no thermal energy, the shielding would be perfect, as there would be the same amount of charge in the cloud as in the primal particle. Consequently, no electric field would be observed in plasma outside the cloud. If the temperature is finite and there is a thermal motion, particles in the edge of the cloud have enough thermal energy to escape the electrostatic potential well. The edge, where the electric field is weak, appears at the radius where the potential energy of particles is equal to their thermal energy. The shielding is not utter, so a finite electric field caused by $k_B T/e$ potential can exist in the plasma. Shielding distance or thickness of such a charged cloud is called the Debye length and is defined as [2]

$$\lambda_D = \sqrt{\frac{\varepsilon_0 k_B T}{n_e e^2}} \quad (1.1)$$

where T is the temperature in K, k_B is the Boltzmann constant in J/K, n_e is electron density in m^{-3} , e is electron charge in C and ε_0 is dielectric constant (F/m). For

example, for the temperature $T = 1 \text{ keV} = 11600 \times 10^3 \text{ K}$ and the electron density of 10^{21} m^{-3} the Debye length is $\lambda_D = 0.2 \text{ }\mu\text{m}$.

The ions and the electrons can often have different temperatures in the plasma. It happens since the energy transfer by collisions between electrons and ions themselves is higher than the one between an ion and an electron. Moreover, other processes in plasma endure for a shorter time, than thermalization process do. The temperature of plasma used in definition is usually the electron one, as the electrons are faster than ions because of their smaller mass. Moving so as to surround an excess of positive charge or repulse from the excess of negative charge they mainly do the shielding. So, when the plasma size L is much greater than the Debye length λ_D , local charge concentration or external potential applied to the plasma is shielded in a short distance compared with L , and the plasma extends without any large electric fields or potentials. The following equation for electric potential in the plasma on the distance r demonstrates this effect [2]

$$\phi(r) = \phi_0 \exp\left(-\frac{r}{\lambda_D}\right) \quad (1.2)$$

where $\phi_0 = \frac{e}{4\pi\epsilon_0 r}$ is the Coulomb potential. So, it is clearly seen, than in the plasma in comparison to vacuum, the potential is exponentially damped with the strength of damping given by the Debye length.

Since the plasma is quasineutral, densities of electrons and ions are in an equilibrium $n_e \simeq Zn_i \simeq n$, where n is a common density called *the plasma density* and Z is the average charge of ions.

The number of particles in Debye sphere is denoted by N_D and is called *plasma parameter*. It can be calculated as [2]

$$N_D = n_e \frac{4}{3} \pi \lambda_D^3 \simeq 1.36 \times 10^6 T^{\frac{3}{2}} n_e^{-\frac{1}{2}} \quad (1.3)$$

Debye shielding is valid only if is large enough, i.e. $N_D \gg 1$.

1.1.2 Plasma frequency

As it was mentioned above, particles in plasma exhibit collective motions. If some electromagnetic wave, e.g. laser pulse, interacts with the plasma, electrons are slightly dislocated from their initial positions while ions are almost at rest due to their larger mass. This charge separation is responsible for a restoring force as it generates an uniform electric field. Consequently, the plasma is subjected to oscillations with frequency [2]

$$\omega_p = \sqrt{\frac{n_e e^2}{m_e \epsilon_0}} \quad (1.4)$$

that is the electron plasma frequency, caused by electron motion, the most rapid one in the plasma. If $\omega_p \gg \nu_c$, where ν_c is the frequency of binary collisions, than collective motion in the plasma prevails over binary interactions.

When the following conditions are satisfied:

1. $\lambda_D \ll L$
2. $N_D \gg 1$

3. $\omega_p \gg \nu_c$

the plasma is called *ideal*:

1.2 Propagation of laser wave in plasma

Laser pulse is an electromagnetic wave. A dispersion relation of the electromagnetic wave propagating in plasma is [3]

$$\omega^2 = \omega_p^2 + c^2 k^2 \quad (1.5)$$

where k is the wave vector, ω denotes the frequency of electromagnetic (EM) wave (laser frequency) and ω_p the plasma frequency 1.4.

Depending on the ω of the laser wave, 3 cases may take place:

- $\omega > \omega_p$, k is real and the wave propagates through the plasma. The plasma is called *underdense plasma*.
- $\omega < \omega_p$, k is imaginary and the wave is exponentially shielded. It propagates into the plasma only until a finite depth - the collisionless skin depth $l_s = \frac{c}{\omega_p}$. In this situation the plasma is called *overdense*.
- $\omega \simeq \omega_p$, $k \simeq 0$, the wave is reflected. The electron density in this case is called *critical density* and is calculated as [4]

$$n_{cr} = \frac{\varepsilon_0 m_e}{e^2} \omega^2 = 1.1 \times 10^{15} m^{-3} \left(\frac{\lambda}{1 \mu m} \right)^{-2} \quad (1.6)$$

So, the critical density distinguishes between the underdense plasma regime and the overdense plasma regime.

In relativistic case an increase of the cut-off density occurs. It means, that if electrons' velocity is near the speed of light in vacuum, the laser wave can propagate even through the overdense plasma. This phenomenon is called a relativistic self-induced transparency.

A parameter which determines whether the electron motion is relativistic or not is the dimensionless amplitude a_0 of the vector potential A in the Coulomb gauge [5]

$$a_0 = \frac{eE_0}{m_e \omega c}, \quad (1.7)$$

where ω stands for the angular frequency of the electromagnetic wave and E_0 is the strength of the electric field. If $a \ll 1$, the case is non-relativistic, i.e. $\gamma_e \approx 1$, where the latter is a relativistic factor of the electrons oscillating in the laser field

$$\gamma_e = \frac{1}{\sqrt{1 - \frac{v_e^2}{c^2}}}. \quad (1.8)$$

For linear polarization the relativistic factor of laser field can be expressed via the dimensionless amplitude [6]:

$$\gamma = \sqrt{1 + \frac{a_0^2}{2}} \quad (1.9)$$

and if the electron is initially at rest, then $\gamma_e \approx \gamma$. On the other hand, $a_0 \geq 1$ indicates that electrons oscillate with a relativistic velocity.

Turning back to relativistic transparency, the reason of this phenomenon is that in this occasion the electron density is corrected by a factor $1/\gamma$. So, in this regime the following inequality is valid [7]:

$$n_{cr} < n_e < \gamma n_{cr} \quad (1.10)$$

explaining the increase of the cut-off density for laser propagation in plasma.

Charged particle motion in electromagnetic field is governed by the Lorenz force:

$$\vec{F}_l = q \left(\vec{E} + \vec{v} \times \vec{B} \right), \quad (1.11)$$

where \vec{B} denotes the magnetic field, \vec{E} is the electric field, v is the velocity and q is the charge of a particle.

Besides the Lorenz force, electrons experience so called ponderomotive force which is caused by the electric field inhomogeneity. This force tends to push the electron against the gradient of slowly-varying averaged laser electric field until the ponderomotive potential Φ_{pon} is compensated by the electrostatic potential Φ_{el} between the replaced electrons and ions. Ponderomotive force can be expressed as [8]

$$F_{pon} = -m_e c \nabla \langle \gamma \rangle = -\frac{\omega_p^2}{\omega^2} \nabla \frac{\epsilon_0 \langle \vec{E}^2 \rangle}{2} \quad (1.12)$$

where $\langle \gamma \rangle$ denotes relativistic factor averaged over the fast laser field oscillations and $\langle \vec{E}^2 \rangle$ is averaged laser electric field.

1.3 Absorption of laser radiation in plasma

Absorption mechanism of electromagnetic radiation is a process in which the energy of a photon is transferred to the matter electromagnetic wave interacts with. Laser light on the short time scales interacts mainly with electrons, as it was mentioned in the previous section, hence laser radiation energy is transferred to plasma via electrons which then pass it to ions.

One of the main characteristics of a laser pulse is the laser intensity. It determines whether the absorption of the pulse by plasma proceeds mainly through collisions of plasma particles or through other mechanisms. If the laser intensity is low ($\leq 10^{17} \text{W/m}^2$), absorption will be mostly collisional. Inverse Bremsstrahlung mechanism is an example of collisional absorption: electron gains its kinetic energy from oscillating laser wave and is subsequently thermalized by collisions.

With the increase in electron temperature collision frequency decreases. It happens because at high intensities ($\geq 10^{19} \text{W/m}^2$) electron motion in the laser field is relativistic, whilst collisional frequency between ions and electron is in inverse ratio to the electron velocity v^3 [8]:

$$\nu_{ei} = \frac{3Z^2 e^4 n_i \ln \Lambda}{8\pi \epsilon^2 m_e^2 v^3}, \quad (1.13)$$

where $\ln \Lambda$ is the Coulomb logarithm and Z is the ion charge number. So, other absorption mechanisms which do not depend on collisions become dominating.

1.3.1 Resonant Absorption

This mechanism lies in resonant excitation of electron plasma wave which then propagates into the overdense plasma. If the laser wave is obliquely incident on the target at some angle θ , it will propagate only up to the density named turning point, where it is reflected (Fig.1.1). The turning point is shifted from the critical density towards lower densities [9]:

$$n_{turn} = n_{cr} \cos^2 \theta \quad (1.14)$$

If the wave is p-polarized, some of its energy tunnels to the critical density surface. In this case electric field \vec{E} lies in the direction of the density gradient, therefore it can resonantly excite electron plasma (Langmuir) wave in the critical layer by separating positive and negative charges.

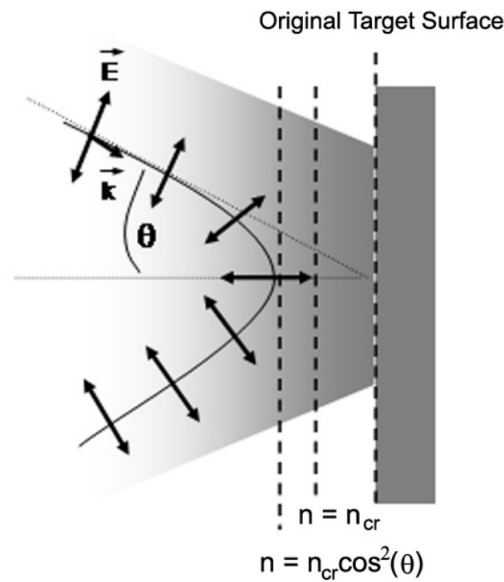


Figure 1.1: P-polarized laser wave of oblique incidence at some angle θ will propagate only up to the turning point [9].

1.3.2 Vacuum Heating

This type of absorption was firstly described by Brunel in 1987 [10] therefore it is also known as *Brunel heating*.

In this scenario, a p-polarized laser wave is obliquely incident on the plasma with a steep density gradient and the electron oscillation amplitude exceeds its scale length. Electrons in the plasma-vacuum boundary are pulled out to the vacuum under the influence of the laser pulse electric field. When the field changes its direction during later phase of one cycle of the laser wave, accelerated electrons reenter the plasma. Since the laser field is attenuated in the overdense plasma, electrons can propagate inside the plasma, and a part of the laser energy they carry is completely scattered in the plasma. Stages of this process are depicted on Fig.1.2.

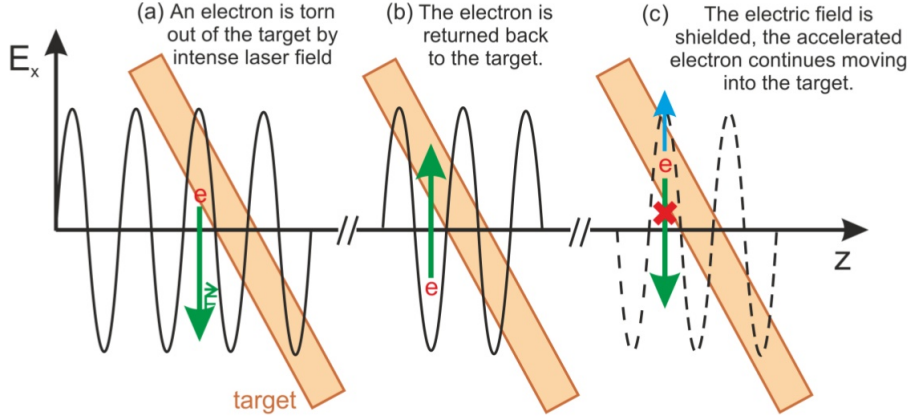


Figure 1.2: Stages of Brunel heating process [7].

1.3.3 Relativistic $\mathbf{j} \times \mathbf{b}$ Heating

The mechanism of $\mathbf{j} \times \mathbf{b}$ heating reminds Brunel vacuum heating. While in the latter one electrons were driven only by the electric field, in the case of electrons oscillating in the laser wave with relativistic velocities the magnetic component of the Lorenz force (1.11) becomes significant. Thus, electrons are extracted into vacuum twice during the laser period by combination of the electric field and the magnetic field, whereas in Brunel heating only once. The advantage of this mechanism is that due to the magnetic component it can be efficient even with perpendicular incidence of the laser pulse or in the case of s-polarized laser wave.

1.4 Mechanisms of laser-driven acceleration of ions

Nowadays laser-driven particle acceleration in plasma is a promising candidate for replacing conventional large acceleration systems such as cyclotron or synchrotron. These accelerators are used for different purposes in various areas from nuclear physics to tumor treatment, and their history counts more than 70 years of developing and enhancement [11]. However, each cyclotron or synchrotron has definite break down limit. To overcome it and to reach higher energies, rebuilding towards bigger size of construction is required, which is impractical from economical point of view.

On the contrary, laser-driven accelerators are compact, as they are able to accelerate particles over only a few micrometer distances, having shorter pulse duration [12]. Also there is no break down limit for the maximum energy in comparison to conventional ones. Moreover, any kind of particle can be accelerated with the help of laser-driven accelerator. The target, which is employed as a particle source, can be easily changed with respect to required ions.

Although laser-driven accelerators possess undisputed advantages, there are some limitations to be overcome. For instance, achieving monoenergetic particle beam and high repetition rate are required to let laser-driven accelerators be competitive with conventional ones in the manner of beams quality. More information about the limitations

can be found in [11].

Let us now turn to mechanisms of laser-driven acceleration. According to (1.15), the acceleration of ions to relativistic velocities ($v_i \sim c$) by direct interaction with a laser pulse would require $a_0 \approx 2000$, or laser intensities more than 10^{24} W/cm². This value is unachievable with current technology, as intensities only up to 10^{22} W/cm² are possible by now [13], [14].

$$\frac{v_i}{c} = \frac{Zm}{M} a_0 \quad (1.15)$$

Nevertheless, laser energy can be efficiently transferred to plasma electrons via various mechanisms discussed in previous section. As a result, a strong quasi-neutral field is generated by charge separation of electrons with respect to ions that can subsequently accelerate ions to high energies. It is worth noting, that e.g. in vacuum this process is impossible, as laser-irradiated ions remains essentially still.

Typical femtosecond laser pulse consists of a main pulse and a so called prepulse, or pedestal, which precedes the main pulse because of amplified spontaneous emission (ASE). Usually, the prepulse intensity has to be much better than 10^{-9} times the intensity of the main pulse (so called *laser contrast*) in order to avoid ionization of the target and on the other hand not to destroy the target before the arrival of the main pulse. When the laser contrast is small, the pedestal is intense enough to create a preplasma sheath expanding into vacuum. As a result, the main pulse interacts with the preplasma, not directly with the target. In order to improve the temporal laser contrast up to few orders of magnitude, an optical device called Plasma Mirror (PM) is often used [15],[16] (the final contrast should be at least 10^{-10}). The PM is a plate of a dielectric material covered with an anti-reflected layer, where the laser beam is focused. When the low-intense prepulse is incident on this layer, it will be transmitted without damaging on the PM surface. With the increase of the laser pulse intensity, the critical plasma can be created on the surface of PM, which reflects the most part of the main pulse like a metallic mirror.

Depending on the target and the laser properties, different ion acceleration mechanisms can intervene.

Two main regimes, Target Normal Sheath Acceleration (TNSA) and Radiation Pressure Acceleration (RPA), that were studied theoretically and experimentally over the past two decades [17], [18] will be briefly described in the following sections. Fig.1.3 shows the comparison of these mechanisms with another acceleration regimes depending on the laser intensity and pulse duration.

1.4.1 Target Normal Sheath Acceleration (TNSA)

The principle of TNSA was firstly suggested by Wilks et al. in 2001[19] and now it has become the most experimentally investigated and widely used mechanism of ion acceleration.

The laser pulse irradiating the target transfers its energy into the hot electrons, which then penetrate through the target. Target is usually a foil in the micrometer thickness range [4]. Once hot electrons reach the target rear surface they create a Debye sheath (with the scale of Debye length). The charge separation results in formation of a strong electric field at the target rear, that instantly ionizes atoms. Subsequently, ions start to expand into vacuum in the sheath field following the electrons, mainly

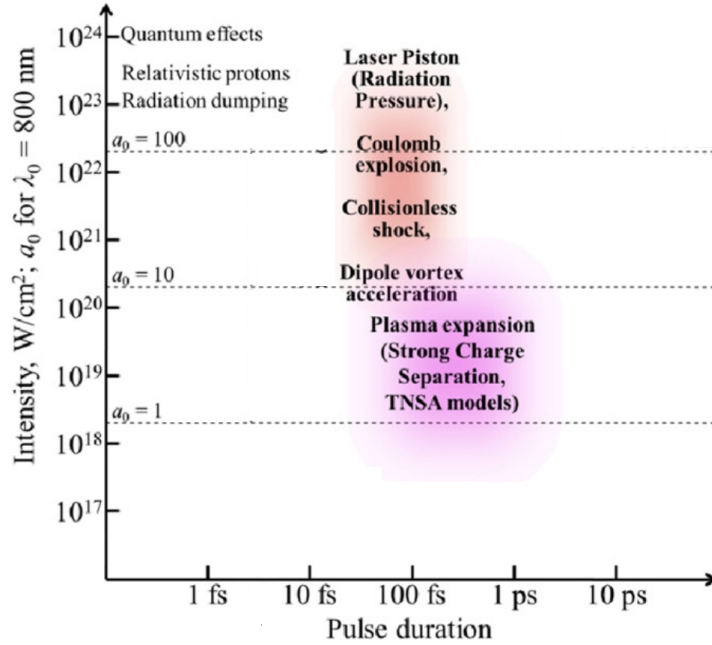


Figure 1.3: Different regimes of laser ion acceleration in plasma depending on the laser intensity and pulse duration, including TNSA and RPA that are sketched in this section. The regimes have no abrupt borders and can overlap with each other. In this graph electron density $n_e = 460n_{cr}$ is supposed in a fully ionized carbon for $\lambda_0 = 800$ nm. ([5], modified).

in the target normal direction. Most of the electrons, however, are pulled back to the foil, as their energy is not high enough to escape their self-induced field. They continue transferring their kinetic energy to ions by recirculation in the foil. Some of them reaches the front target surface and generate a sheath field accelerating ions in opposite direction. As the number of electrons outside the foil remains almost constant, an equilibrium is established. The ion acceleration continues as long as the laser heats electrons. The simplified scheme of the TNSA is on the Fig.1.4.

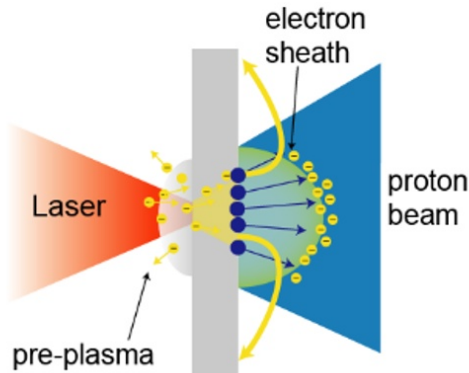


Figure 1.4: Scheme of the Target Normal Sheath Acceleration [21].

Among other ions, protons can be most efficiently accelerated due to their high charge-to-mass ratio. The highest published TNSA proton energy so far is 85 MeV [1].

According to TNSA theoretical model presented in [20], some relations can be proposed. The predicted number of ions per unit energy and unit surface (energy spectrum) is given by

$$\frac{dN}{d\varepsilon} = \frac{n_{i0}c_s t}{\sqrt{2\varepsilon Z k_B T_e}} \exp\left(-\frac{2\varepsilon}{Z k_B T_e}\right) \quad (1.16)$$

where ε denotes the ion energy and $c_s = \sqrt{Z k_B T_e / m_i}$ the ion acoustic velocity, Z is the ion charge number, k_B the Boltzmann constant, T_e the electron temperature and m_i is the ion mass. The maximum ion energy is derived as

$$\varepsilon_{max} = 2Z k_B T_e [\ln(2\tau)]^2 \quad (1.17)$$

where $\tau = (\omega_{pi} t_{ac}) / (\sqrt{2} \exp(1))$ and ω_{pi} is the ion plasma frequency, t_{ac} stands for the ion acceleration time, n_{i0} is the electron density in the unperturbed plasma.

1.4.2 Radiation Pressure Acceleration (RPA)

Electromagnetic waves can carry momentum, as photons traveling with the speed of light have nonzero momentum although they are zero-rest mass particles. So, any surface irradiated by EM wave is exposed to radiation pressure, i.e. the flow of the momentum per unit surface. Radiation pressure P for a plane monochromatic EM wave of intensity I normally incident on the plane surface of a medium at rest can be expressed as [6]

$$P = (1 + R - T) \frac{I}{c} = (2R + A) \frac{I}{c}, \quad (1.18)$$

where R , T and A are the coefficients of reflection, transmission and absorption.

Esirkepov was first who showed that for laser intensities exceeding 10^{23} W/cm² radiation pressure acceleration (RPA) becomes dominant mechanism of ion acceleration instead of TNSA mechanism [22]. Later research [23] have shown, that RPA is also possible for lower intensities (10^{19} W/cm²), if circular polarization of laser light combined with normal incidence on the target are used. In this case hot electron generation is strongly suppressed, that results in eliminating the TNSA acceleration and maximizing radiation pressure.

The concept of RPA is the following. When the laser pulse impinges the overdense plasma, electrons from plasma surface are pushed inwards by the ponderomotive force, creating a charge separation field. This electrostatic field affects ions and accelerates them in the forward direction.

Depending on the target thickness, two further scenarios can take place [6], [18]. Firstly, if the laser propagates through the foil only until limited depth and does not interact with the target rear side, the target is referred to as the thick one. That leads to the acceleration of part of ions in the target through RPA. This is called the 'hole boring' regime. Secondly, in case of the foil is nm thickness, all ions on the laser path are accelerated as it passes through the entire target, and a slab of the plasma is accelerated as a whole. This regime of RPA is termed as the 'Light Sail' regime. Both cases are pictured in Fig.1.5.

For RPA mechanism being successful, the thin foil target has to be a perfectly reflecting, undeformable plane mirror so that it can be boosted by radiation pressure [14].

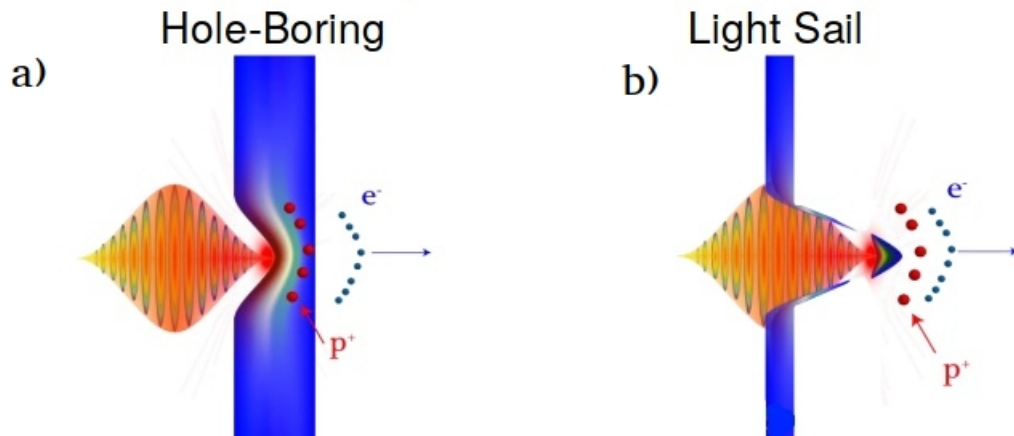


Figure 1.5: Scheme of the Radiation Pressure Acceleration regimes: a) is the 'Hole Boring' regime and b) is the 'Light Sail' regime. [24].

Chapter 2

Detection of accelerated ions from plasma

In order to be successfully employed in multidisciplinary fields (e.g. in proton therapy, in biological application, in Nuclear Physics, in Science of the Matter), laser-accelerated ion beam ought to be properly characterized in terms of maximum energy, number of particles, shot to shot reproducibility and spatial distribution, the most important beam parameters.

The aim of this chapter is to introduce diagnostics capable measure these characteristics. The main focus will be set on the real-time diagnostics working in the TOF configuration. The most commonly used devices will be described here, including Faraday cup and semiconductor detectors. At the end of the chapter alternative detectors, such as Thompson parabola and RCF films, will be described.

2.1 Time-of-flight detectors

TOF technique is a method that can provide information about ions generated by the laser-to-target interaction. It has been an effective diagnostic tool for many years [25]. TOF efficiency in the measurements of ion beam characteristics such as species, current, energy spectrum, intensity and also shot-to-shot reproducibility has been showed in many published works [26], [27], [28].

One of the advantages of this detection method in comparison to others, is its ability of being employed in real time. So, it is possible to monitor the ion current distribution and control the energy of the beam in real time during the experiment. Thanks to that possibility, changes in experimental setup, such as change of the detector's distance or angle to the target or adding/removing filters in front of the detector and so on, can be easily realized. The TOF technique principle is to determine the ion's velocity and energy distribution via a time measurement.

After being accelerated, ions continue their moving in the vacuum chamber until they reach the detector. The acceleration is implemented via some of the regimes, two of which (TNSA and RPA) were described above. The detector is located in a certain distance from the target (i.e. particle source). While ions are traveling through the vacuum, their velocities remain almost unchanged. During the journey, particles are separated into groups according to their velocity. So, the lightest ions come first to the

detector, followed by heavier ones. Since one knows the target-detector distance d , and ion's flight-time t , the ion velocity can be easily calculated as

$$v = \frac{d}{t}; \quad (2.1)$$

and subsequently the kinetic energy of the ion is

$$E = \frac{mv^2}{2} = \frac{md^2}{2t^2}, \quad (2.2)$$

where m is the ion mass, v is the velocity and t is a measured TOF t_{tof} corrected onto the detector distance from the target as follow:

$$t = t_{tof} + \frac{d}{c}, \quad (2.3)$$

where c is a light speed.

A typical TOF spectrum (see Fig.2.1) consists of a relatively long photopeak, induced by XUV and visible radiation coming from the laser to target interaction, fast ions peak and a broad heavy ions peak. According to the photopeak the start of the signal can be determined. In some cases the photopeak overlaps with the fast ions peak in the TOF spectrum, hence it becomes hard to distinguish between them. It is possible to increase the detector-target distance in order to solve this problem, but the further distance leads to a decrease of the signal amplitude. So, different approaches how to minimize the XUV emission were developed, e.g. the use of semiconductor detectors, filtering metal foils, etc. [25], [27]. In the next sections the most commonly used detectors operating in TOF configuration will be described.

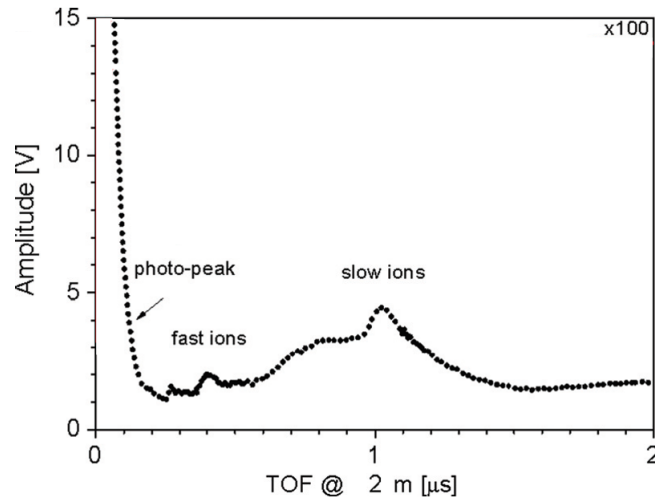


Figure 2.1: Typical ToF spectrum obtained by Faraday cup. In this case fast ion peak consists of protons and slow ion peak of silicon ions with different charge states. ([25], modified)

2.1.1 Ion collector

The ion collector, also called as Faraday cup (FC), is basically a small cup composed of two insulated electrodes, that collects ions and converts their charge to the current that can be measured. Consequently, the total number of impinging particles can be estimated. The electric field created between two FC electrodes contributes to separating ions from electrons. In order to detect positive charges, the inner electrode has to be negatively polarized. The outer electrode is grounded and operates like a shield of the inner one, protecting it from radiation and charged particles coming from sides. The ion beam impinges on the inner electrode through the thin window and hits the metal. Since the electrode is a part of the electric circuit, it gains a small net charge while ions are neutralized. The inner electrode is afterwards discharged and the current is recorded by a fast storage oscilloscope. The scheme of the Faraday cup is shown in Fig.2.2.

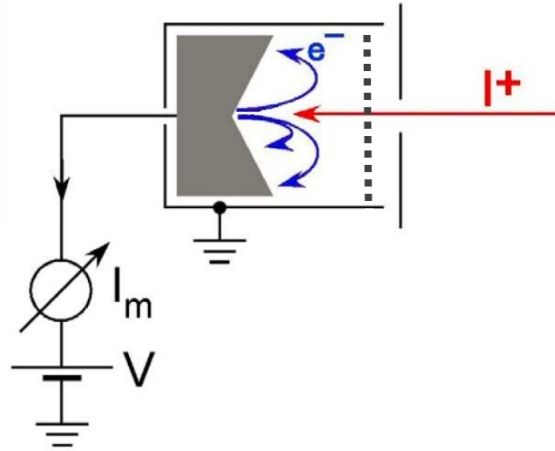


Figure 2.2: Scheme of the Faraday cup, [29].

Despite the relatively simple principle, ion collector appears to have complications in practice. The issue is that, when the charged high-energetic particles interact with the electrode, undesirable secondary electron emission is induced. As electrons leave the surface, the positive charge on the cup becomes overestimated, that leads to discrepancy in the current. Also, electrons produced due to the photoemission upon impact of XUV plasma radiation outside the cup can permeate inside it and cause the same effect as inner secondary electrons. Nevertheless, different solutions have been developed. Firstly, production of the cup with a material generating less free electrons under the impact of the ion beam. Secondly, combination of magnetic and electric fields with different cup shapes in order to confine electrons to ion collector [27]. To filter out XUV component and reduce generation of outer electrons, thin metal foils are placed before the cup [25].

2.1.2 Semiconductor detectors

This type of detectors uses a semiconductor to measure properties of impinging radiation. Main composition parts of such detectors are active region, constituted by intrinsic or low-doped (with introduced impurities) semiconductor, and junctions located at two sides of the semiconductor. When impinging particles interact with the detector active layer, they can induce a production of electron-holes pairs, provided that their energy is large enough to overcome band gap. Energy gap or band gap of a semiconductor is an energy required to turn a valence electron bound to the atom into a conduction electron, which is capable to move freely within the crystal lattice and operate as a charge carrier to conduct electric current. At the same time, equal number of holes created in the valence band also act like carriers. Reversed bias is applied on junctions, resulting in generation of electric field in the detector depletion region. Under the influence of this electric field electrons and holes are drifting in opposite directions to the electrodes, where they produce a current pulse that is detected and integrated. The output voltage is proportional to the radiation energy, as the number of produced electrons and holes (e-h) is proportional to it.

Due to their structure, such devices demonstrate a lot of advantages in comparison to other types of detectors working in TOF configuration. For instance, high speed of response, ensured by the high saturation velocity of charge carriers in semiconductors, permits to recognize even fast particles. If the band gap is higher, than the impinging photons energy, it is possible to cut visible and infrared radiation. Also, semiconductor detectors are able to operate under harsh radiation conditions, as the process of e-h pairs creation is fully reversible and undamaging. But a non-ionizing energy can influence the crystal lattice and hence impede the motion of charge carriers, reducing the height of outcome voltage amplitude. Nevertheless, right concentration of dopant in active layer allows to control this process [30]. High charge collection efficiency of such detectors allows to use them in time-of-flight configuration. Among other benefits are also room temperature operation and high signal-to-noise ratio.

Characteristics of a semiconductor detector are different depending on the experiment it is manufactured for and also according to what is commercially available. Two most commonly used semiconductor detectors, Silicon Carbide(SiC) and Diamond Detector (DD) will be described in next sections.

2.1.3 SiC detector

Nowadays silicon carbide detector (SiC), developed in the last decade, is of a big interest in the laser-plasma diagnostics, as it shows very interesting features such as high charge collection efficiency, fast collection time and resistance to high radiation fields. Also, the SiC detector has the lowest dark currents noise among various semiconductor detectors [31],[26].

There are different technologies of building SiC detectors. Generally, it has a PN (PIN) diode or metal-semiconductor junction structure, which operates under a reverse bias. One of the possible constructions of the SiC detector is pictured in the Fig.2.3. This device was built starting from the 4H-SiC wafer containing a residual n-doping. Undoped epitaxial layer which was grown on a n-type doped active layer acts as a detector active region. Ohmic contact covers all the back surface of the wafer, whereas

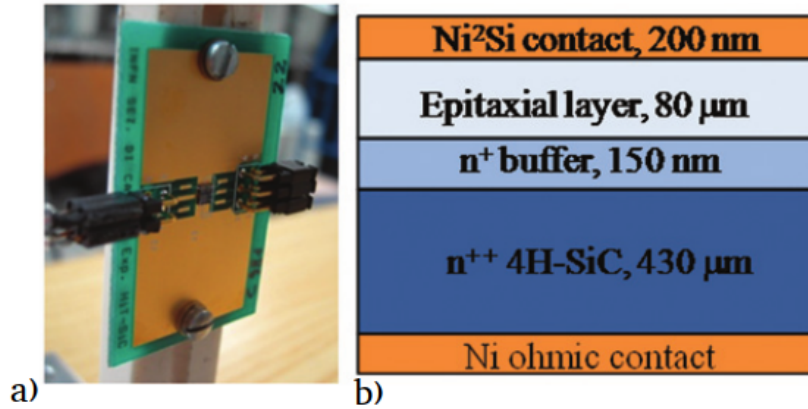


Figure 2.3: Picture (a) and sketch (b) of the structure of the SiC detector.[25]

a metal-semiconductor Schottky junction (realised with Ni₂ Si layer) is fabricated on the epitaxial layer side.

The signal measured by using a SiC detector is proportional to the ion energy released into the detector active layer. It happens since the incident ions, after being absorbed by the layer, produce there electron-holes pairs, losing 7.8 eV for pair production. The higher the energy of the ions, the more e-h pairs are produced, therefore the detector sensitivity will grow with the increasing energy of the incident particles.

Moreover, due to the large band gap (3.2 eV) of such detectors, plasma-emitted UV and visible light radiation is highly attenuated, hence it allows to separate the plasma fast ion peak from the photopeak, usually consisted of XUV component. So, it is possible to detect X-rays and fast ions at the same time. The presence of X-rays in the signal is important for its evaluation and the data analysis, as they indicate the beginning of the measured signal, i.e. location of X-ray peak is considered as a zero point for TOF calculations. The Fig.2.4 illustrates that the photopeak is strongly lowered in comparison to fast ions peak, whereas the photopeak from the Faraday cup signal disallows us to distinguish fast ions. Moreover, in case of SiC the photopeak is very narrow, while the one measured by FC is relatively broad.

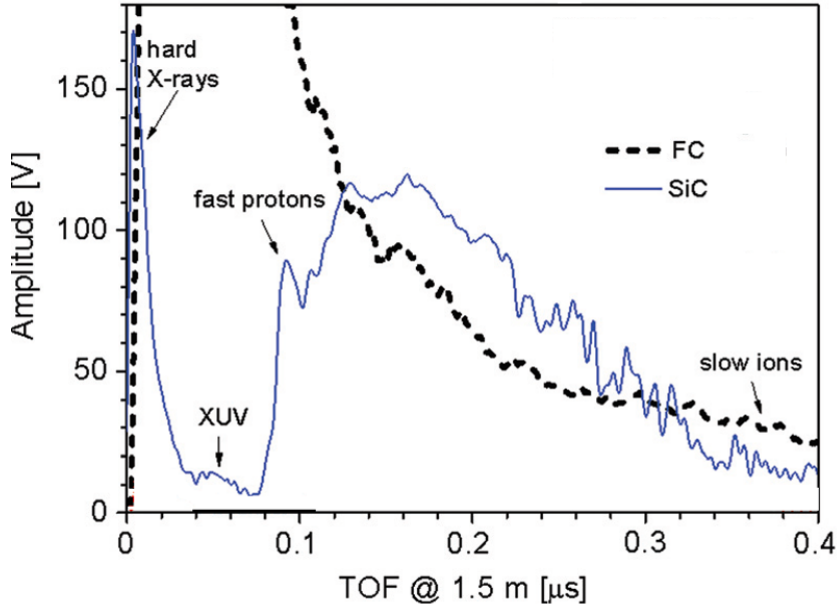


Figure 2.4: Comparison between signals obtained by Faraday cup (FC) and by SiC detector. Laser energy $E_l = 594$ J and SiH target were used in this shot. ([25], modified)

2.1.4 Diamond detector

Diamond detector (DD) is another type of semiconductor device, having many similarities with SiC detectors, but much more expensive and difficult to be manufactured [32]. Their main advantages are fast charge collection time thanks to high mobility of charge carriers, low leakage current, high radiation resistance and high operating temperatures as well. Also, DD is able to operate under high temperature, as the melting point of diamond is very high (4363 K).

A diamond film, representing the detector active layer, is grown using the chemical vapor deposition (CVD) process. It is equipped with ohmic contacts in both sides, forming a detector. When the external voltage is applied between contacts, an electric field emerges. Charge carriers, produced as a result of impinging radiation, travel in this field and induce a current in the external circuit. In fact, many charge carriers do not finally reach electrodes due to trapping and recombination processes that take place in CVD diamond, therefore only the length of their path contributes to the signal [33].

Due to the large band gap 5.48 eV diamond detector is not sensitive to visible light, so, similarly to SiC, it is able to distinguish high energetic particles emitted from the plasma. But on the other hand charge collection efficiency of diamond detector is quite low, as e-h generation is significantly smaller compared to other materials. Nonetheless, this problem can be solved using appropriate amplifier. Furthermore, large energy gap enables detector to operate without depletion by a reverse bias voltage, as the dark current is negligible.

The Fig.2.5 demonstrates the schematic structure of the diamond detector with the scheme of the used electronic circuit. Charge sensitive amplifier (CSA), which is symbolized as an operational amplifier with a feedback capacitor, reads out the induced charge on the electrodes and produces a voltage output proportional to it [34].

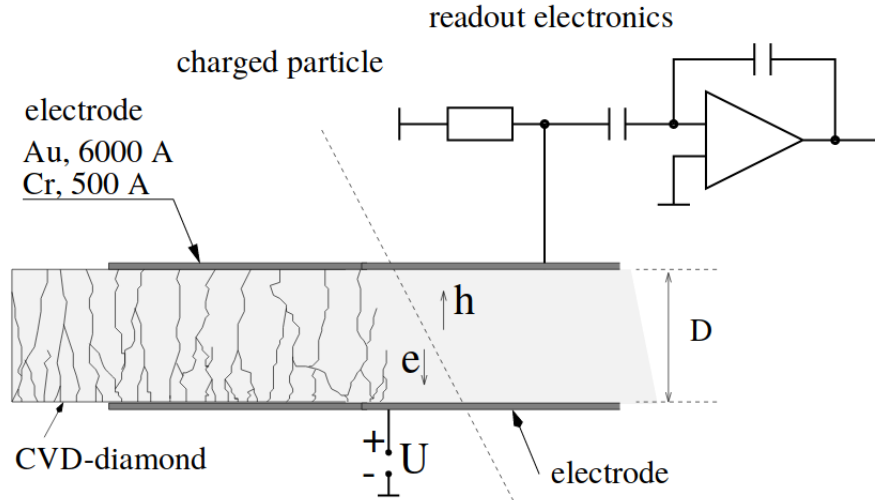


Figure 2.5: Principle of diamond detector. U is bias, applied to the electrodes, D is the thickness of the detector (the distance between the electrodes) [35].

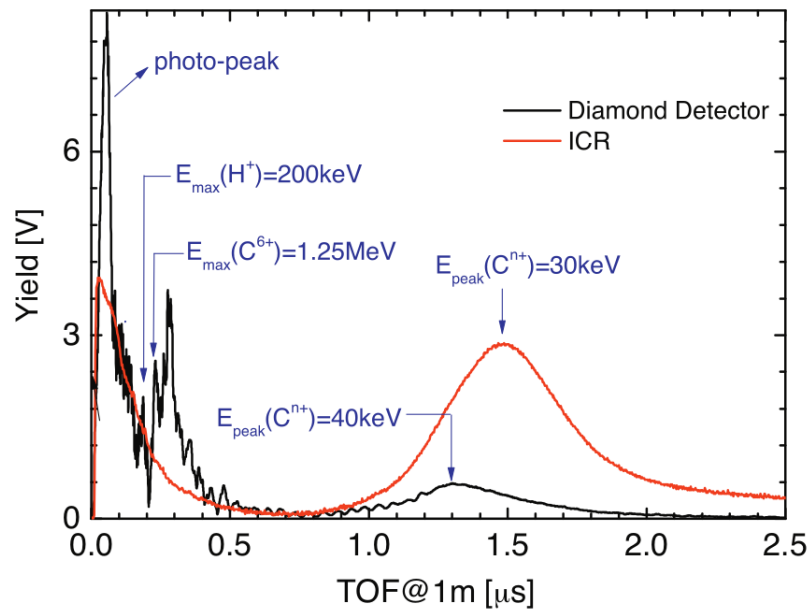


Figure 2.6: Typical diamond TOF spectra for diamond and ion collector obtained by ablating thin mylar target at PALS laboratory in forward direction ([28], modified)

The comparison between TOF diamond spectra and ion collector spectra is represented in Fig.2.6. It is clearly seen, that the ion collector signal linked to fast protons and

ions (H^+ , C^{6+}) is completely hidden by the 'tail' of the photopeak, whereas diamond detector allows to efficiently distinguish fast particles peaks, as they are well separated from the photopeak. In contrast, slow ions signal (C^{n+}) is well discerned in IC respond, whilst in case of DD the signal is very low.

So, it is possible to conclude, that the use of semiconductor detectors is very efficient to measure fast protons and fast ions, as special properties of such devices allow these peaks to come out of the strongly lowered photopeak. Faraday cup (Ion collector) is instead more sensitive to slow ions, while in case of using semiconductor detectors their signal can be very low. It happens, because the signal of latter detectors is proportional to the energy deposited in their active layer. Moreover, the ohmic layer of these detectors, used for the electric circuit, filters out low energetic particles and therefore cuts the certain part of the signal.

Thereby, simultaneous use of semiconductor detectors and ion collectors can provide one with complementary information about plasma products [25].

2.2 Thomson parabola

Thomson parabola spectrometer (TPS) is a diagnostic tool for characterizing multi-species energetic ion beams. With the help of TPS it is possible to observe energy spectra of different ion species and their charge states by separating them according to the charge-to-mass ratio of the particular particle. Because of this feature TPS is complementary to other diagnostics in most laser-plasma experiments [36],[37].

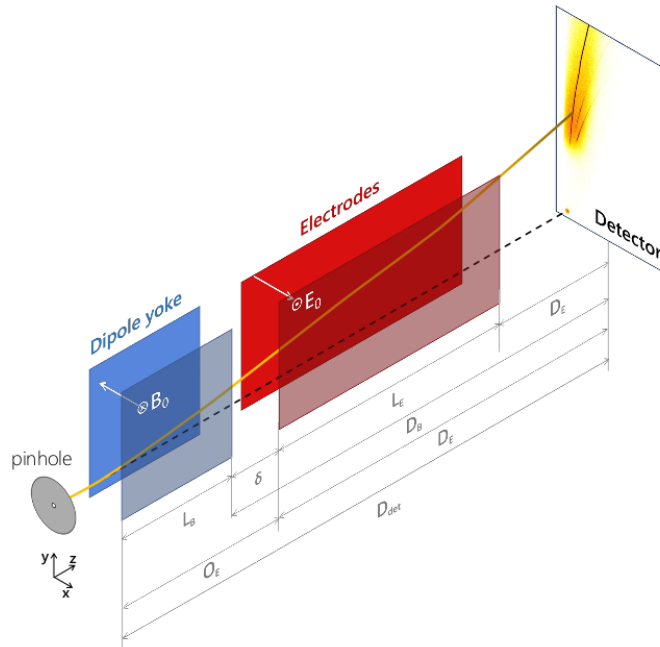


Figure 2.7: Thompson parabola spectrometer scheme. The yellow line illustrates ion motion and the black dotted line is the trajectory of X-rays and visible light through static magnetic and electric fields [36]

Ion separation occurs thanks to the combined use of static electric and magnetic fields, which are generated by potential difference across a pair of electrodes and by a pair of permanent magnets or powered by appropriate current coils respectively. Fields are parallel to each other and perpendicular to the motion of the particle beam. An example of TPS is showed in Fig.2.7. The pinhole at the entrance selects a pencil beam of ions which then travel through the fields. The magnetic field, which is set first, deflects charged particles along the y-axis (the direction, perpendicular to both magnetic field and particles velocity), according to the magnetic term of Lorentz force:

$$\vec{F}_m = -q\vec{v}_z \times \vec{B}, \quad (2.4)$$

where q denotes particle charge, v_z speed along z-axis and B is the magnetic field.

Under the influence of the electric field E , particles are deflected along the x-axis. According to the electric term of Lorentz force, positively charged particles are deflected in the direction of the field E , while electrons are pushed oppositely:

$$\vec{F}_e = qE. \quad (2.5)$$

Passing through the fields, charge particles obtain a curved trajectory - parabola (hence the name), that is finally recorded on an imaging plane. The recording plane of TPS is usually represented by an imaging plane.

For non-relativistic speeds ($v_z \ll c$) and for Larmour radius larger than the magnet length, a parabolic trace of particles of a given $\frac{q}{m}$ can be described by expressions[38]

$$x = \frac{qBL_B}{mv_z} \left(\frac{L_B}{2} + D_B \right); \quad y = \frac{qEL_E}{mv_z^2} \left(\frac{L_E}{2} + D_E \right), \quad (2.6)$$

where m is a particle mass, L_B and L_E are lengths of the magnetic and electric field, D_B and D_E are distances from the magnet and electrodes to the detector respectively. So, ions with different charge-to-mass ratios are separated in different parabolas. The signal received on the detector along particular parabola can be converted to an energy spectrum by the use of these equations.

Although TPS has been an efficient diagnostic tool in mass spectrometry since the time of J.J.Thomson [39], with the recent evolution in laser technologies TPS ought to undergo different modifications in order to solve three main problems arising during their use in experiments. First, as the position of parabolic ion trace is a function of charge-to-mass ($\frac{q}{m}$) ratio, ions with the same $\frac{q}{m}$ will have their parabolas fused on the imaging plane. Nevertheless, if one needs to distinguish lightest ions between species with the same $\frac{q}{m}$, a stepped Differential Filtering (DF) technique can be employed, as described in [37]. This technique consists in using a stack of foils of different materials and thickness, ordered so as to block the propagation of heavy ions while discriminating the light ones.

Second problem is overlapping of high-energy ion tracks. It happens since energetic particles are only slightly deflected by the fields. The most effective solution of this issue is enlarging the electrode length by applying trapezoidally shaped electric plates [36]. With such electrodes, the high-energy particles will travel in longer electric field region in comparison to slower ones, and subsequently will be deflected more. Slower ions will be able to cross over the wedged side of the electrode.

The lack of spatial information of the ion beam that is induced by the necessity of the pinhole is the last problem with TPS described here. One of the ideas is to substitute the pinhole by horizontal slit, that was performed in [40].

2.3 Radiochromic films

Radiochromic film is a plastic film that is capable to change its color upon exposure to ionizing radiation. The advantage of this film type over other types (photographic) is that no chemical processing is required to develop an image. Color of RCF becomes dark blue, as the active layer of this film presented by radiation-sensitive organic microcrystal monomers undergoes polymerization process when exposed to radiation. Established polymer in turn changes the color. Darkness of the film is proportional to the absorbed dose of radiation.

To obtain as much information about the beam as possible, radiochromic films are put together forming a stack detector [41]. RCF layers alternate with metal (Al or Fe) layers, that act as shielding. When the ion beam goes through, each layer stops particles of definite energy interval (because of the Bragg peak), resulting in RCF in the stack are darkened gradually. The information about maximum ion energy, an approximate energy spectrum and the number of particles can be obtained by analyzing those imprints on films. A scheme of an example of RCF stack covering energies up to 62.2 MeV is shown in Fig.2.8, while particular RCFs with imprints after the irradiation are depicted in Fig.2.9.

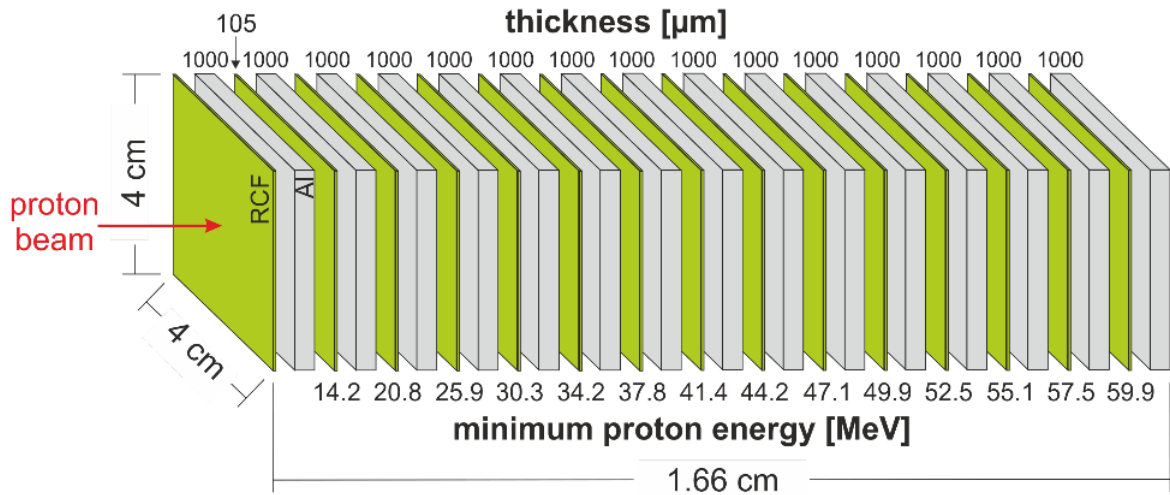


Figure 2.8: Example of RCF stack detector used to measure proton beams, [7].

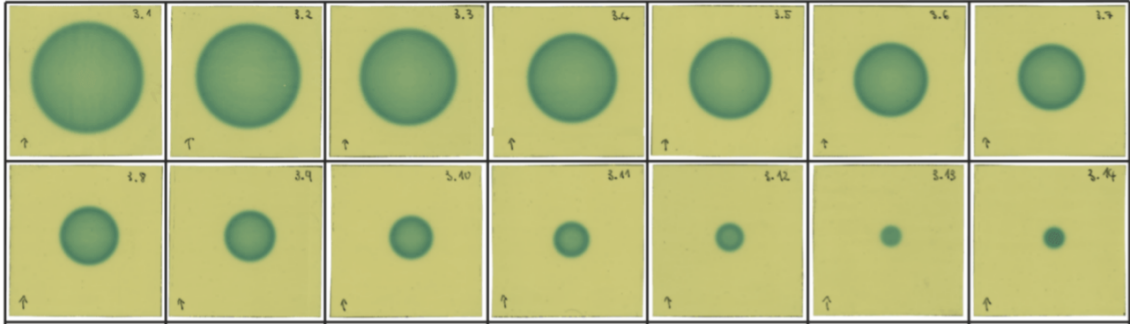


Figure 2.9: RCF with imprints of a spatially modulated proton beam. The first film in the stack is shown on the top left and the last one is in the bottom right, [7].

Moreover, unlike TOF detectors and TP, that can catch only a fraction of the accelerated ions, such detector provides high spatial resolution information about the distribution of radiation, as every film plays a role of 2-D map of the absorbed radiation.

However, it is not a real-time diagnostics. The development of the film after irradiation lasts for few days, leading to a necessity of waiting to obtain reliable information about the beam. Furthermore, sometimes it is difficult to distinguish between electrons, ions and X-rays, as RCF are sensitive to any type of radiation. In this case an appropriate filtering system is required. Additionally, a deep data analysis has to be implemented to distinguish different particles.

Nowadays various models of radiochromic films under a GafChromicTM brand name are widely used [42].

Chapter 3

Experiments and data analysis

Despite the fast progress in laser-driven particle acceleration in last decades, a lot of efforts have to be done yet in order to improve ion beam characteristics, such as enhancing the maximum energy and the number of particles, improving the shot to shot stability and beam homogeneity. A lot of experiments are carried out with this purpose, refining existing and developing new approaches to the improvement of these characteristics.

In this chapter I am going to describe two different experiments and show the analysis of some experimental data implemented by myself. The first experiment was aimed to investigate how the use of nanostructured targets influences the laser absorption (which in turn can influence the maximum energy and the amount of generated protons) and the second one intended to increase the yield of generated alpha particles by triggering the proton Boron (pB) nuclear fusion reaction. The focus of this thesis will be on the first experiment.

The deconvolution technique, used to interpret the signal from the working in TOF configuration detector, and the experimental setup of each experiment will be also described in next sections, followed by the analysis of some data from experiments.

3.1 Technique of deconvolution

Using TOF detectors during an experiment will provide information about the current and energy of ions generated after the laser-target interaction. In order to determine main parameters of the ion beam, such as the energy distribution and the number of particles of each charge state or ion group, the measured spectrum has to be deconvolved by the use of an appropriate function.

Since the motion of the particles is well described by means of a Maxwell-Boltzmann shifted function, the latter one can be applied on the spectrum to recover velocity peaks of different ion species and charge states contributions. This function takes into account only brief collisions between particles, when they exchange their energy and momentum, and the system of particles is assumed to have reached thermodynamic equilibrium. It depends on the temperature of the system and the mass of the particle [43]:

$$i(t) = \frac{d^2}{t^5} \exp \left[-\frac{m_i}{2k_B T} \left(\frac{d}{t} - v_s \right)^2 \right], \quad (3.1)$$

where $i(t)$ is the ion current, d the distance between the target and the detector, m_i the ion mass, k_B the Boltzmann constant, T the ion temperature, t the time of flight, and v_s the ion shift velocity caused by the plasma center-of-mass velocity and by the quasielectrostatic field acceleration. This Gaussian function gives the probability of finding a particle with a speed v at time t .

The observed ion current is the sum of partial currents of all the ionized species. So, if the spectrum is deconvolved by means of a Maxwell-Boltzmann shifted (MBS) function, taking into consideration every ion and its charge states, the resultant curve will approximate the original spectrum.

However, before to do a deconvolution of the signal by applying MBS functions, some modifications with the original signal, recorded by using an oscilloscope, have to be carried out.

1. The amplitude of the signal has to be regulated so that the baseline matches with the zero line. Sometimes it has to be also multiplied by a factor, called a reflection coefficient Γ^1 .
2. The time axis has to be corrected by adding the time employed by the light to reach the detector (see Eq.(2.3)).
3. The time axis has to be shifted so as to have the photopeak, which indicates the beginning of the signal, at zero point.

To apply MBS function, we also have to know which kind of particles should be expected in particular experiment. Right interpretation of the signal according to these kinds is important as well. Since the lightest and hence the fastest ions are protons and the highest velocity means the shortest time-of-flight, the first peak is usually attributed to them. Heavier ions, that are slower than protons, constitute the main peak of the signal. Species of these ions depend on the target material.

Usually several MBS functions are used to fit the spectrum. These functions are plotted using different values of velocities that slightly differ from each other. The velocities can be calculated from the time related to the peak. The temperature value used in these functions should be the same or differ just slightly, because it appertains to the plasma during the laser-plasma interaction. Also it is necessary to multiply each MBS function by a normalization factor, that will correct the height of the function. The sum of these curves approximates the original signal.

For proton deconvolution, several functions of different velocities are often used to approximate the proton peak, that is explained by a presence of protons of different energy in the peak. On the other hand, for ion deconvolution the maximum of used MBS functions is determined by the number of ion charge states.

¹ When the signal is too intense, we need to use an attenuator, connected with the measuring device (oscilloscope). This electronic device lowers the amplitude of a signal of a factor Γ without distorting its waveform in order to protect the measuring device from damage. The reflection coefficient can be calculated with the help of Eq.(3.2), where RL is the known return loss attenuator coefficient expressed in dB [44]

$$RL [\text{dB}] = 20 \log_{10} \Gamma. \tag{3.2}$$

Once the total deconvolution curve is plotted, we can calculate the ion energy E using Eq.(2.2) and then obtain the energy distribution: dependence dN/dE on E , where N stands for the particle number. That will provide an important information about the maximum energy and the number of the ions. Expression dN/dE is computed as

$$dN/dE = \frac{E_g V}{e R E^2} (0.5t - dt), \quad (3.3)$$

where E_g is the minimum energy to create the electrone-hole couple inside the detector, e is electron charge, R is resistance in the oscilloscope, V is the measured voltage, dt is oscilloscope sampling time and t is recorded time. To calculate the number of particle N , expression (3.3) should be integrated by E .

Finally, we have to check if the results are consistent with the reality. Based on the known laser parameters (intensity, pulse duration), experimental setup and target components, values of energy and number of particles are expected to be in certain ranges.

3.2 Experiment at Lund Laser Center

Let us consider ions laser-accelerated in the TNSA regime, one of the most studied acceleration mechanisms. The energy of accelerated particles is proportional to the electric field. The field is created by the charge separation, as hot electrons, generated during the laser-target interaction, penetrate through the target. The number of hot electrons and hence the strength of the field is partially determined by the fraction of the absorbed laser energy in the irradiated target. Therefore, enhancing the laser absorption can lead to the increase of the ion energy and the number of accelerated ions. One of the possible ways to increase the laser absorption is the use of a thin (submicron thickness) foil covered by nanostructures as a target, as it was successfully demonstrated in several theoretical and experimental papers [45], [46]. The benefits of using such targets were recently demonstrated in an experiment that was performed at Lund Laser Center (LLC) in Sweden in 2016 with a TW laser system [47].

Various types of detectors were used during this experiment to characterize the beam of accelerated particles, e.g. a magnetic spectrometer and RCF stacks. In this thesis data only from single crystal diamond detector (SCDD) working in TOF configuration will be analyzed.

Also, several types of targets were employed in order to compare results and to get complementary information about the use of nanostructured targets.

Thin plastic (MylarTM) foils of 500 nm thickness were covered by monolayer of polystyrene nanospheres with diameter of 400 nm on the front (laser-irradiated) or rear side. The first ordering allowed a small enhancement of the maximum energy, the number of the accelerated protons and the beam homogeneity, while the second one changed only the spatial distribution of the beam. Nanospheres targets were fabricated at the ELI Beamlines target laboratory according to the technique described in [47], [48]. Flat plastic foils (MylarTM or polyethylene terephthalate (PET)) were used as reference targets, having the same overall thickness (900 nm) as nanosphere type.

In this thesis, we will concentrate on the data obtained after the laser interaction with the front side nanosphere and the flat target, so it will be possible to compare

both results. Fig.3.1 shows the picture of the nanosphere target obtained by Scanning Electron Microscope (SEM).

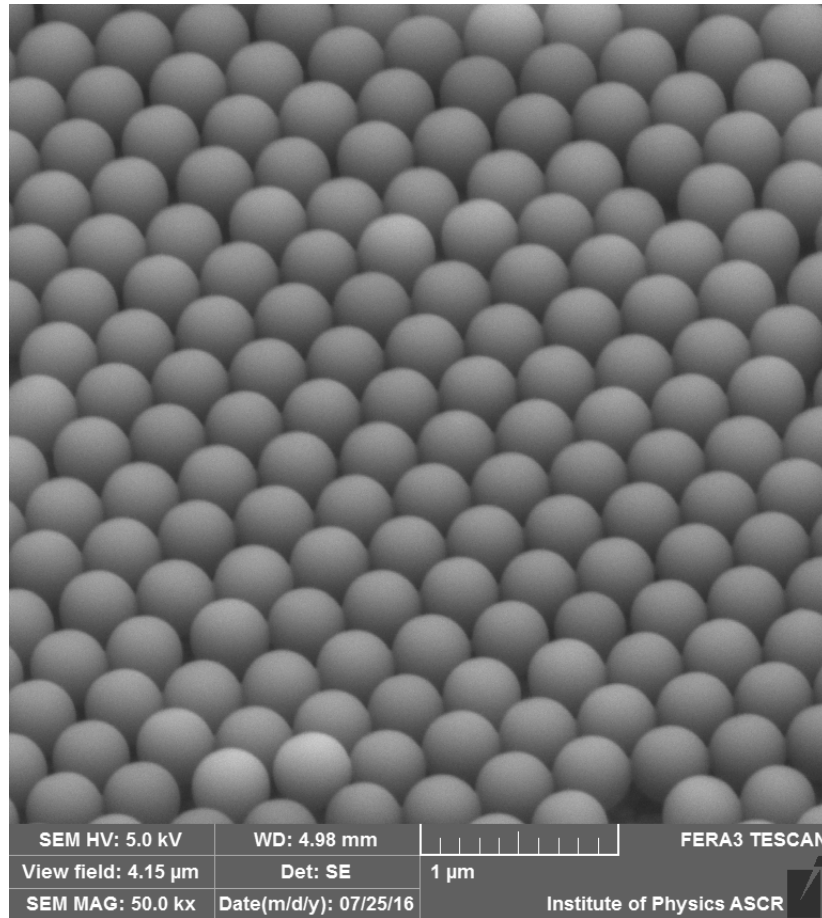


Figure 3.1: PET target covered with nanospheres [47].

3.2.1 Experimental setup

A Ti:sapphire laser system is available at LLC facility. The laser works in a single shot or at a repetition rate of 10 Hz. The central wavelength of the laser is 800 nm. During the experiment it delivered 2 J of energy per pulse before compression and approximately 1 J after the compression. The pulse duration after the compression was 35 fs and the laser focal spot was measured to be around $3.5 \mu\text{m}$. The pedestal, caused by ASE, was originally of the order of 10^{-9} at 120 ps prior to the main pulse. Since the nanosphere target front surface had to remain undamaged by pedestal before the main pulse arrives, a plasma mirror (PM) was used to improve the laser contrast. As a result, temporal contrast ratio was enhanced by approximately two orders of magnitude. Also, off-axis parabolic focusing mirror (OAP) was used to focus the laser beam on the target. Eventually, the laser intensity on the target reached $4 \times 10^{19} \text{ W/cm}^2$.

A hyper pure $4.4 \times 4.5 \text{ mm}^2$, $500 \mu\text{m}$ thick, single crystal diamond detector (SCDD) was placed behind the target at a distance of 56 cm and an angle of 9° with respect to

the target normal. This detector was employed in time-of-flight configuration, allowing to control proton current and energy distribution in real time. Fig.3.2 shows a sketch of the experimental setup.

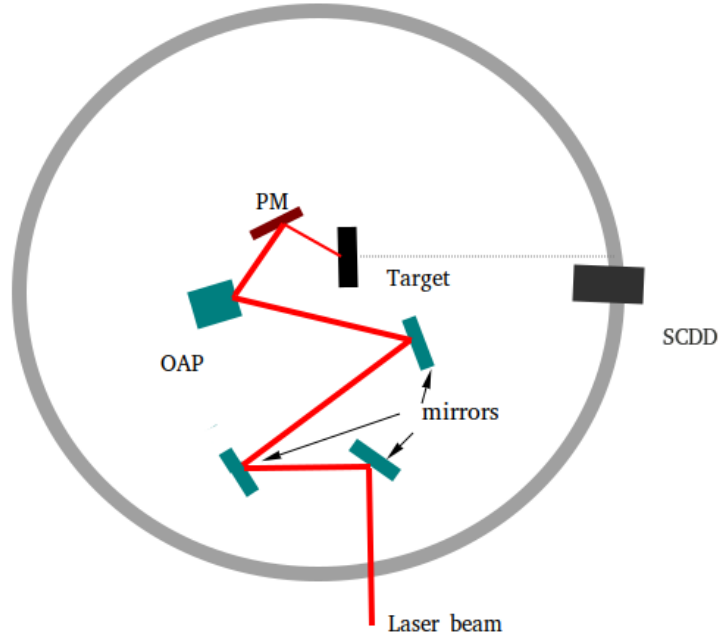


Figure 3.2: Sketch of the experimental setup at Lund Laser Center. SCDD stands for the single crystal diamond detector, OAP for the off-axis parabolic focusing mirror and the PM for the plasma mirror.

3.3 Data analysis

In this section, two successful shots from LLC experiment are analyzed. During the implemented analysis, I applied theoretical knowledge from the previous chapters in practice. I used the same spectra as were described in Ref.[47] so that I could compare my results with published ones. In the case of shot 9, flat mylar target (PET) was used, whereas in shot 12 nanosphere target covered by nanostructures irradiated from the front side was employed.

Deconvolution process was accomplished with the help of Matlab program. According to the theory, a model of a deconvolution script was optimized to make it appropriate for my analysis and deconvolutions for each of the following shots were performed. During the data analysis we were interested only in proton distribution, therefore only the first peak of the TOF spectra is deconvolved.

3.3.1 Shot 9: Mylar target

Fig.3.3, a) shows the TOF spectrum obtained after the laser interaction with PET target. It is immediately noticeable, that the photopeak, indicating the beginning of

the signal, is very small. This is due to the use of diamond detector, as reduction of the photopeak is one of its advantages. Consequently, the fast protons peak can be easily distinguished, as it does not overlap with the photopeak. Also, no extra UV or X-ray radiation contaminates the spectrum. Furthermore, the recorded spectrum shows very low signal-to-noise ratio.

As can be seen as well, the first peak is well-distinguishable from the rest of the signal, because of the distance between the target and the detector, enough for ion separation. The rest of the recorded spectrum is an ion component signal. It is containing several charge states from different ions components, such as Si, C, N, O and others.

Fig.3.3, b) depicts the original signal including the deconvolved signal obtained by using the technique described in section 3.1. As the interest was only in protons, I deconvolved the first peak to four partial peaks applying expression (3.1). Velocities were chosen in the range $(1.69 - 2.02) \times 10^7$ m/s and the temperature of 10^8 K. Every function was multiplied for an appropriate normalization factor. These four functions are represented by blue dotted gaussian-form curves in the figure. All parameters used for the deconvolution are reported in the Table3.1. The resultant curve, which is depicted in blue, approximates the experimental peak. It is very important to control if the beginning of the peak coincides with the beginning of the deconvolution curve, as it can influence further analysis (e.g. energy distribution). The beginning of the first peak is approximately at 24.3 ns, so the maximum energy of 2.7 MeV can be expected.

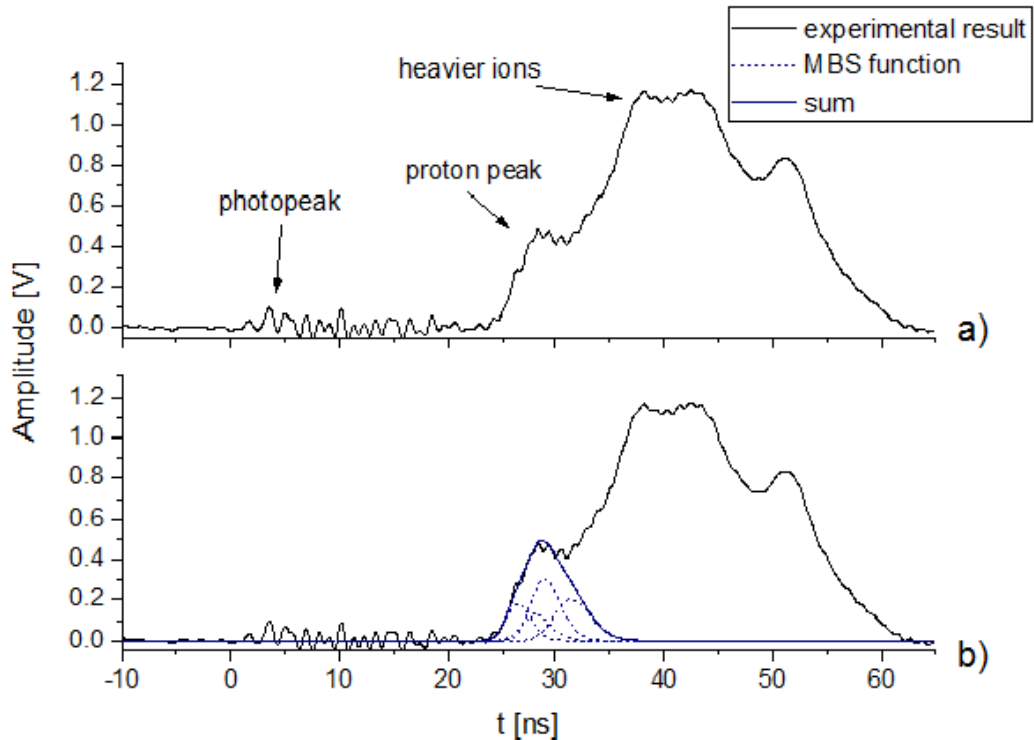


Figure 3.3: Original (a) and deconvolved (b) TOF ion current distribution, shot 9.

N [-]	$v_s \times 10^7$ [m/s]	$T \times 10^8$ [K]	$A \times 10^{-38}$ [-]
1	1.69	1.00	2.20
2	1.84	1.00	2.20
3	1.90	1.00	0.81
4	2.02	1.00	0.81

Table 3.1: Parameters used for proton deconvolution of the signal of the shot 9. N stands for a MBS function number, v_s is a proton shift velocity, T is a temperature and A is a normalization factor.

The energy distribution of protons is presented in Fig.3.4. According to the plot, it can be estimated that the maximum energy reaches 2.7 MeV. This value coincides with the expected one. It is evident from the plot, that the number of low energetic protons exceeds the amount of high energetic particles.

The total number of protons having energy more than 1 MeV measured by the detector was calculated by integration of the Eq.3.3 as $N_p = 1.3 \times 10^6$.

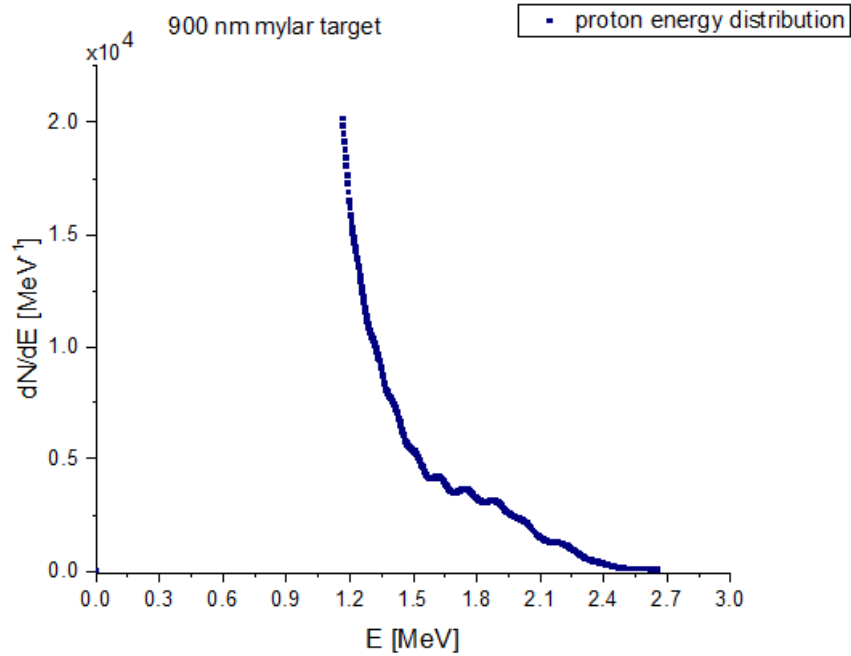


Figure 3.4: Proton energy distribution for the shot 9.

3.3.2 Shot 12: Mylar + Nanosphere target

In this shot another type of target was used – front-side nanosphere target. As can be seen from the plot (Fig.3.5, a)), that causes different laser-plasma interaction products, than in the previous shot. Similarly to the the first shot, the signal is well-distinguishable and with small photopeak, thanks to the diamond detector. In that instance, there are

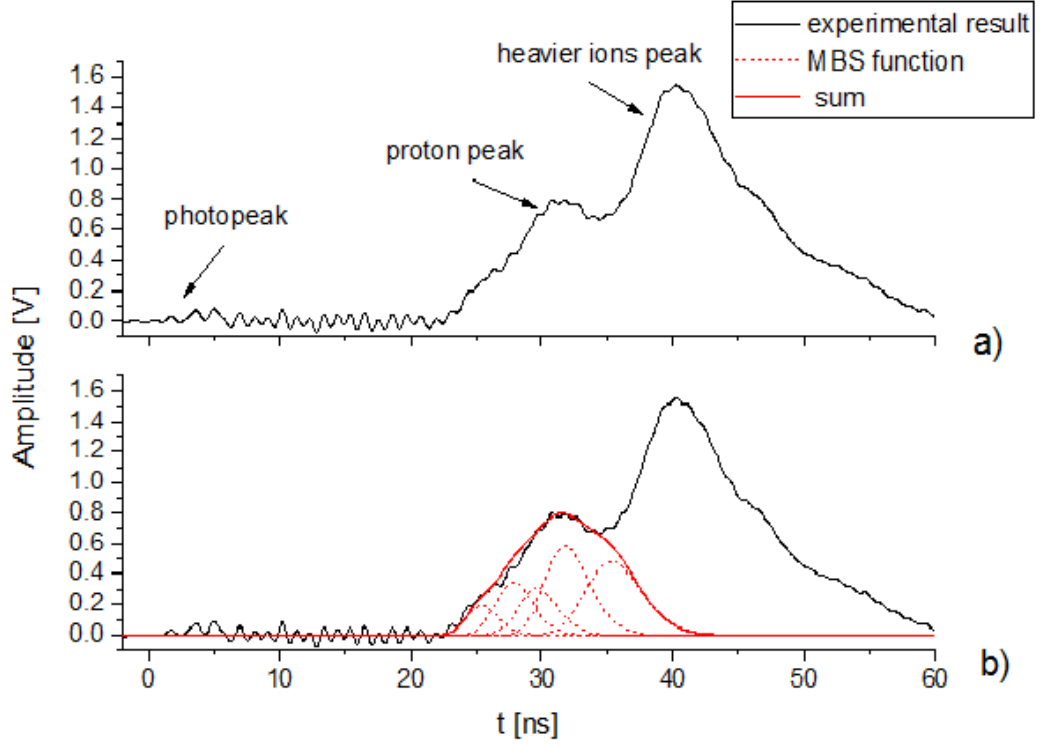


Figure 3.5: Original (a) and deconvolved (b) TOF ion current distribution, shot 12.

only two discernable peaks, indicating the presence of two ion species: protons, constituting the first peak, and heavier ions associated with the second one.

To approximate the peak as best as possible, five MBS functions were used. The right localization of these functions tended to be difficult, as even a little change in parameters of one of the functions induced changes of the total curve. Eventually, the velocities were chosen between $(1.50 - 2.11) \times 10^7$ m/s and the temperature was 10^8 K. For more details about used parameters see Table 3.2.

The Fig. 3.5, b) shows the deconvolved spectrum, red dotted curves represent deconvolution curves and the red one is their sum, likewise in the previous graph.

N [-]	$v_s \times 10^7$ [m/s]	$T \times 10^8$ [K]	$A \times 10^{-38}$ [-]
1	1.50	1.00	9.50
2	1.67	1.00	6.80
3	1.80	1.00	2.50
4	1.92	1.20	2.00
5	2.11	1.20	0.70

Table 3.2: Parameters used for proton deconvolution of the signal of the shot 12. N stands for a MBS function number, v_s is a proton shift velocity, T is a temperature and A is a normalization factor.

Preliminary value of the maximum proton energy is 2.9 MeV, since the first peak starts at approximately 23.1 ns. The energy distribution of protons for this shot is shown in Fig.3.6. In that case the energy maximum reached the value of 2.9 MeV and the number of protons having energy more than 0.9 MeV measured by detector was calculated as $N_p = 7.0 \times 10^6$.

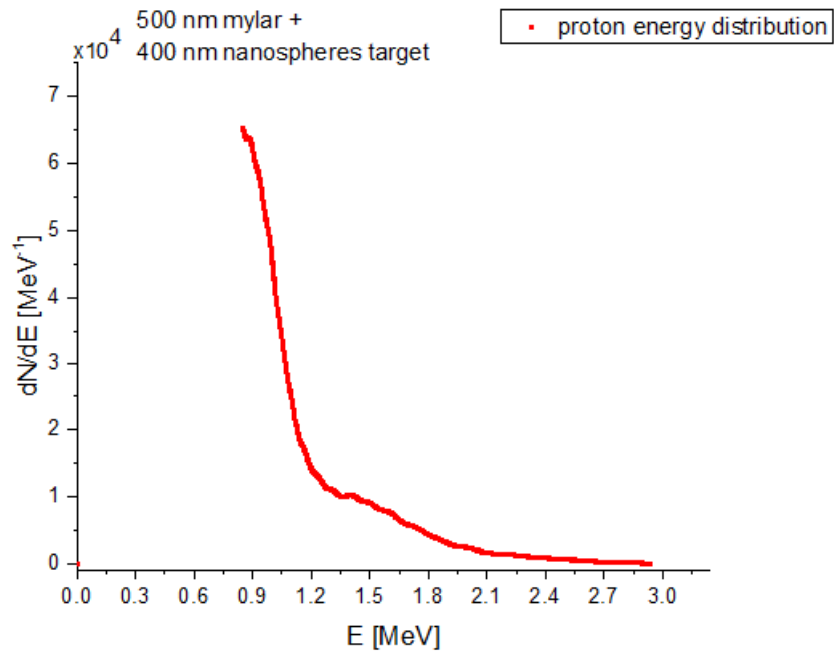


Figure 3.6: Proton energy distribution for the shot 9. .

3.3.3 Comparisons of shots and of obtained and published results

The comparison of proton energy distribution for both shots is shown in Fig.3.7. The vertical axis of this graph is converted into logarithmic scale for illustrative purposes.

As can be seen, energy distributions for the shot with nanosphere target and for the one with reference target are quite similar and differ just slightly. Nevertheless, maximum proton energy reached almost 3.0 MeV in the case of nanosphere target, whereas in the other case it was about 2.7 MeV. Turning to the published results [47], presented in Fig.3.8, we will find almost the same values of energy for both target types as presented in this section. For the shot 9 the maximum energy is 2.8 MeV and for the shot 12 it is approximately 2.97 MeV.

Although the maximum proton energy increased by using the target with NS on its front surface, it was not enhanced considerably. The reason of this can be the large laser-target interaction angle, that was 45° to the target normal. As it was demonstrated in [49], with the increase of angle, the surface of laser interaction with nanostructured target decreases, that results in a decrease of particles energy.

The proton number was higher in the instance of the shot with the nanosphere target. However, to prove that the enhancement happened due to the use of this target type, more shots for each target should to be analyzed.

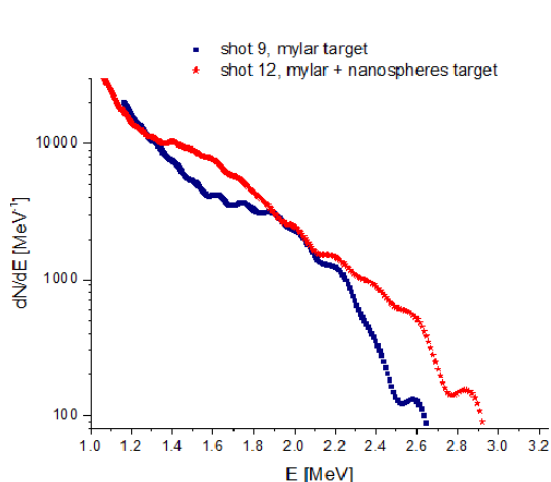


Figure 3.7: Comparison of proton energy distributions for the shot 9 and 12.

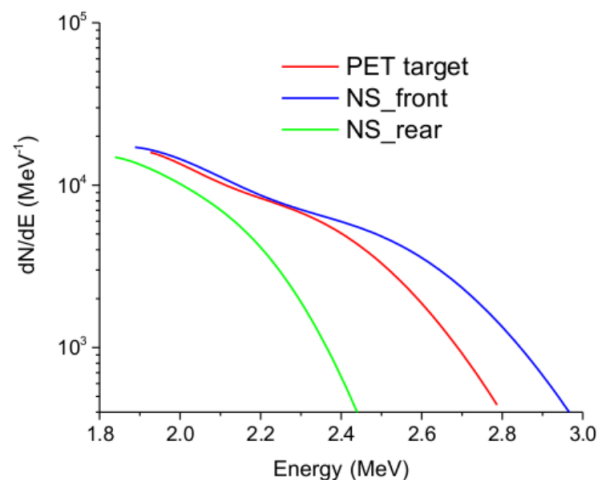


Figure 3.8: Comparison of proton energy distributions for the shot 9 and 12 published in [47].

3.4 Experiment at Prague Asterix Laser System

The second experiment considered in this thesis was performed at Prague Asterix Laser System (PALS) in 2016.

The technique of deconvolution that was described in section 3.1 is general and can be applied to any type of charged particle. For instance, I used it to get the

full deconvolution of the spectra, obtained in the experiment at Prague Asterix Laser System (PALS) performed in 2016.

The aim of this experiment was to trigger the proton-boron nuclear fusion reaction by using an intense laser focused in a solid target containing boron (^{11}B). The final result of this neutron-less nuclear reaction is the generation of alpha-particles according to the following relationship:



The possibility to trigger this nuclear reaction by using an intense ps laser ($2 \times 10^{18} \text{ W/cm}^2$) interacting with a solid polymeric target enriched with boron was experimentally demonstrated for the first time by Belyaev *et al.* in 2005 [50]. An alpha yield of about 10^3 alphas per steradian per pulse has been obtained in this experiment.

A more sophisticated and complicated experiment has been recently performed at Laboratoire pour l'Utilisation des Lasers Intenses (LULI) by Labaune *et al.* [51]. A maximum yield of about 10^7 alphas/st/pulse was achieved using two laser beams: the first with a long pulse (ns range) to ionize the ^{11}B plasma, the second with a short pulse (ps range) and with high intensity (10^{18} W/cm^2) to accelerate the proton beam in the TNSA regime.

Almost simultaneously, Picciotto *et al.* [52] succeed to produce a very high alpha-particle yield per shot around 10^9 st/pulse with an experimental setup close to the one used in [50], but with an advanced target geometry (H-enriched, B-doped silicon) and temporally shaped laser pulse with a much lower intensity (around 10^{16} W/cm^2) at PALS. These results have been demonstrated also with thin targets in the second experiment [53].

Results described in this section are part of a new experimental campaign devoted to the study and to the understanding of this nuclear reaction by using more sophisticated targets. The use of targets enriched with hydrogen and boron was supposed to increase the alpha particles number in this experiment, as was already demonstrated in [?]. The experimental data only from Silicon-Carbide (SiC) detector will be considered here.

The laser pulse energy during the experiment at PALS was 500 J and the pulse duration was 0.3 ns. The nominal laser intensity of $3 \times 10^{16} \text{ W/m}^2$ was reached. Massive silicon samples (0.5 mm thick) were employed as targets. They were implanted with boron atoms located at 190 nm depth with concentration of approximately 10^{22} cm^{-3} . The concentration of hydrogen was about 10^{20} cm^{-3} . Four SiC detectors and four DD were placed at different distances from the target and at different angles to the target normal in order to study the angular distribution of the alpha-particles..

Here the response of two SiC detectors for the shot N50532 (shot reference used at PALS) will be reported. The first detector was located 85 cm far from the target and at 0° to the target normal, while the second one was situated at 66° and at the 136 cm distance. As can be seen from Fig.3.9 a) and b) recorded signals have bigger photopeaks and lower signal-to-noise ratio, than signals obtained with Diamond detector in previous part. In b) case it was difficult enough to find the beginning of the photopeak due to the noise, as the photopeak is relatively low.

As it was expected, these spectra are notably different. It happened due to different detectors angles, because after the laser-target interaction protons were accelerated mainly along the normal to the target, while alpha particles, generated by nuclear reaction 3.4, were distributed almost homogeneously in the space. For comparison

reason, Fig.3.9 shows these spectra normalized to the distance of 1 m. As it can be seen, the beginning of the fast ions peak in a) and the first peak in b) are both at approximately 45 ns.

In this experiment the presence of alpha particles, protons and boron ions was considered in both spectra. Since the angle of the second detector was big, two peaks in b) were considered as alphas with different energies, while in the first spectrum (a)) it was supposed that the slow ions peak is constituted mainly by protons. Fig.3.9 c) and d) depicts the deconvolved signal by means of MBS function. Two blue dotted curves are alpha particles deconvolution with velocities of 2×10^7 m/s and 1.37×10^7 m/s. In this shot, two groups of alphas of different energy were generated during the nuclear reaction. The pink curve is proton deconvolution with 1.68×10^7 m/s velocity and the green one represents borons moving with 1.5×10^7 m/s. The temperature value was in the 10^8 K range. The resultant curve is pictured in red color. All parameters used for the deconvolution are summarized in Table3.3.

It is evident from the plot, that the number of alpha particles do not decrease with the increasing angle from the target normal (in comparison to proton number).

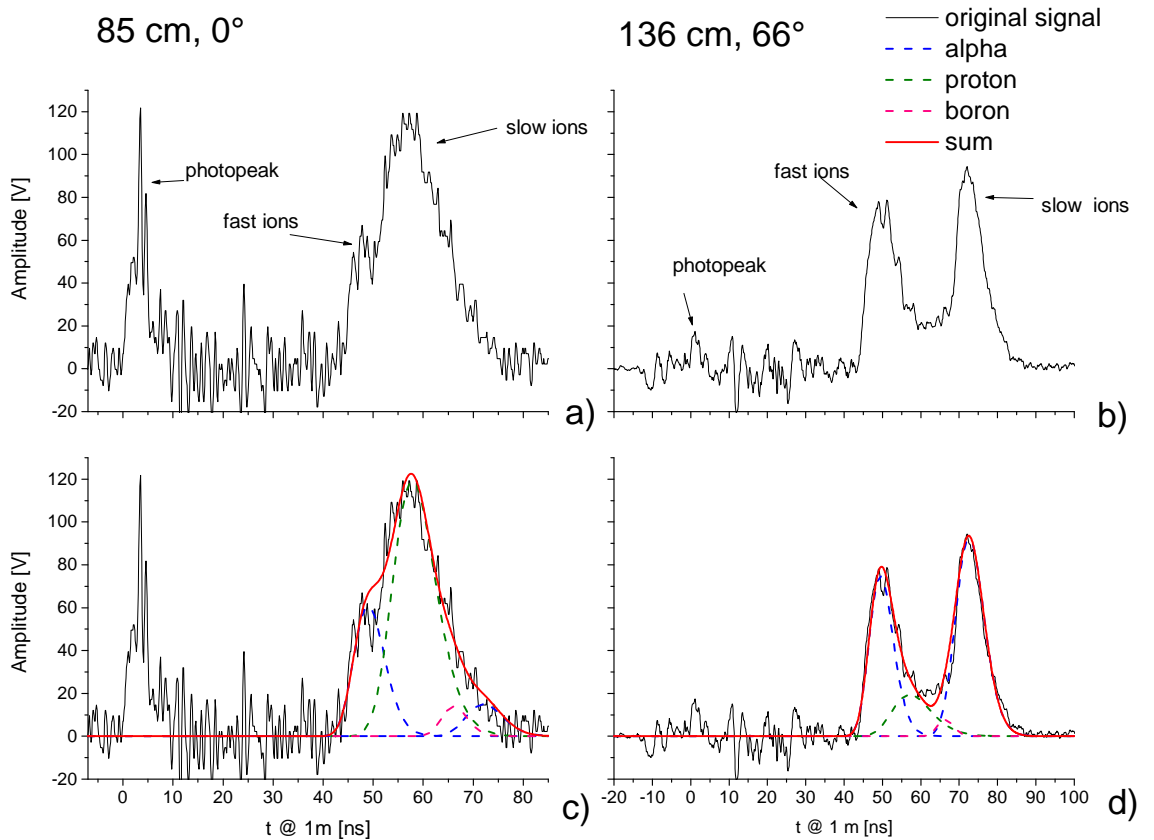


Figure 3.9: Original (a), (b) and deconvolved (c), (d) TOF ion current distributions from two SiC detectors. Spectra are normalized to 1 m distance.

	$v_s \times 10^7$ [m/s]	$T_{85} \times 10^8$ [K]	$A_{85} \times 10^{-35}$ [-]	$T_{136} \times 10^8$ [K]	$A_{136} \times 10^{-35}$ [-]
alpha1	2.00	8.00	1.81	8.00	2.33
alpha2	1.37	2.41	3.00	2.41	19.20
proton	1.68	2.00	8.30	3.00	1.30
boron	1.50	4.50	1.80	3.00	1.30

Table 3.3: Parameters used for alpha, proton and boron deconvolutions of two signals attributed to one shot performed in the experiment in PALS. v_s is a particle shift velocity. T_{85} is a temperature and A_{85} is a normalization factor for the deconvolution of a signal from 85 cm, 0° placed detector, T_{136} is a temperature and A_{136} is a normalization factor for the deconvolution of a signal from 136 cm, 66° placed detector.

The maximum energy of alpha particles, protons and boron ions is determined by the location of the beginning of corresponding peaks in the deconvolved spectra. For protons the maximum energy reaches approximately 2.3 MeV, for borons - 14.5 MeV and for alpha particles - 11.0 MeV. The energy distribution of alphas for both detectors is shown in Fig.3.10. Zoomed region depicts both spectra at high energies. It can be seen that after approximately 11.0 MeV spectra start to oscillate and distribution takes negative values (impossible), so we do not consider energy values more than 11.0 MeV. The energy range 2.5-11 MeV corresponds with expectations (previous results).

The total number of alphas having energies more than 2 MeV, measured by detectors is $N_a = 1.5 \times 10^7$ in case of the normal detector location and $N_a = 6.0 \times 10^7$ in case of 66° angle between detector and target normal. From these calculations and from the Fig.3.9 it is evident, that the number of alpha particles do not decrease with the increasing angle from the target normal (in comparison to proton number). So, it may be concluded that alpha particles are distributed almost homogeneously in the space not following the same rules than ions generated by laser driven acceleration.

Results, obtained in this section, will contribute to the paper that is currently under progress.

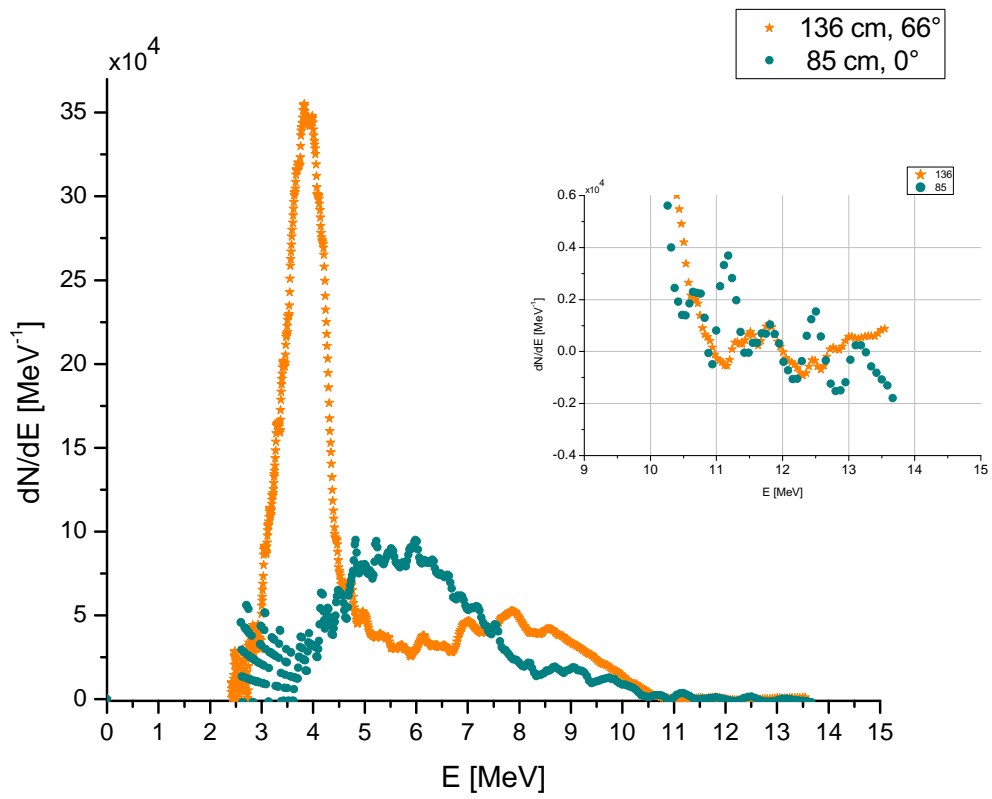


Figure 3.10: Energy distribution of alpha particles for both detectors used.

Conclusion

The basics of laser-plasma interaction and particle acceleration theory were sketched in the first chapter of this thesis. Plasma characteristics and different mechanisms of laser absorption were described, as well as mostly studied laser-driven ion acceleration mechanisms. The goal of the second chapter was to introduce the most widely used types of detectors, especially those working in TOF technique: Faraday cup, Silicon carbide (SiC) and Diamond detectors.

The last chapter deals with the description of two experiments, performed at Lund Laser Center and at Prague Asterix Laser Facility in 2016, and with the analysis of experimental data, obtained with the help of semiconductor detectors, namely with single crystal diamond detector (SCDD) in the first experiment and SiC in the second one. The advantages of using semiconductor detectors for the detection of accelerated ions generated in plasma during the laser-to-target interaction were discussed. The deconvolution technique that I used to carry out the analysis was also described in this chapter. This technique allows to successfully characterize the multi-species ion beam recorded by the TOF detector in terms of ions distribution, maximum ion energy and the ion number.

Two shots with different targets types (nanospheres+mylar and flat mylar targets) from the experiment in LLC were analyzed and subsequently my results were compared with published ones. Only the first peak of both spectra was deconvolved by means of Maxwell-Boltzmann shifted function, as for the final goal of the experiment it was interested only in protons. Proton energy distribution of both shots are in agreement with published results. The maximum energy of 2.9 MeV was achieved while using the nanosphere target, although it does not differ considerably from the one in the flat target case. The accelerated proton number was higher also in the instance of nanosphere target (7×10^6). So it can be assumed, that the use of this target type actually contributed to the enhancement of maximum energy and number of particle.

The fact that the deconvolution technique can be applied to any charged particle was demonstrated in the analysis of data from the second experiment. In this case, I analyzed the responses of two differently located SiC detectors for one shot. I implemented a full deconvolution of two signals, considering alpha particles, boron ions and protons as products of laser-to-target interaction. The maximum energy of alpha particles reached the value of 11.0 MeV, that corresponds with expected values from the pB nuclear reaction. According to the response of the detectors and to calculated number of particles measured by each detector, it may be concluded that during the experiment alpha particles were generated as a consequence of a proton-boron(11) nuclear reaction, instead of laser-to-target interaction.

Semiconductor detectors working in TOF technique appeared to be a reliable tool

in laser accelerated ion characterization, especially regarding the maximum energy and the number of particles. Used in combination with other types of detectors, they can provide with complimentary information about the particle beam, that is important for realization of such applications as e.g. hadrontherapy and nuclear reactions triggering.

Bibliography

- [1] F. Wagner, O. Deppert, C. Brabetz, P. Fiala, A. Kleinschmidt, P. Poth, V. A. Schanz, A. Tebartz, B. Zielbauer, M. Roth, T. Stöhlker, and V. Bagnoud. Maximum Proton Energy above 85 MeV from the Relativistic Interaction of Laser Pulses with Micrometer Thick CH₂ Targets. *Physical Review Letters*, 115(20):205002, 2016.
- [2] F.F. Chen. *Introduction to plasma physics*. 2nd edition, Plenum Press, New York (1984).
- [3] B. Sedlák, I. Štoll, *Elektrina a magnetismus*. Available online at www.jaderny-prvak.8u.cz/wp-content/uploads/2013/02/Sedlak-Stoll-Elektrina-a-magnetismus.pdf, accessed 20.06.2016.
- [4] A. Henig. *Advanced Approaches to High Intensity Laser-Driven Ion Acceleration*. Dissertation thesis, Ludwig Maximilians University in Munich, Germany, 2010.
- [5] H. Daido, M. Nishiuchi, A.S. Pirozhkov. Review of laser-driven ion sources and their applications. *Reports on Progress in Physics*, 75(5):056401, 2012.
- [6] A. Macchi, M. Borghesi and M. Passoni. Ion acceleration by superintense laser-plasma interaction. *Reviews of Modern Physics*, 85(2): 751, 2013.
- [7] Jan Kaufman, *Development of Radiochromic Film Diagnostics for Laser-Driven ion beams*. Master thesis, Czech Technical University in Prague, Czech Republic, 2015.
- [8] Jan Pšikal. *Ion Acceleration in Small-size Targets by Ultra-intense Short Laser Pulses (Simulation and Theory)*. PhD thesis, Czech Technical University in Prague, Czech Republic, 2009.
- [9] Matthew M. Allen. *Ion Acceleration from the Interaction of Ultra-Intense Lasers with Solid Foils*. PhD thesis, University of California, Berkeley, 2004.
- [10] F. Brunel. Not-so-resonant, resonant absorption. *Physical Review Letters*, 59(1):52, 1987.
- [11] K. W. D. Ledingham and W. Galster. Laser-driven particle and photon beams and some applications. *New Journal of Physics*, 12(4):045005, 2010.
- [12] D. B. Zou, A. Pukhov, L. Q. Yi, H. B. Zhuo, T. P. Yu, Y. Yin and F. Q. Shao. Laser-Driven Ion Acceleration from Plasma Micro-Channel Targets. *Scientific Reports*, 7:42666, 2017.

- [13] P. Gibbon. *Short pulse laser interactions with matter: An introduction*, Imperial College Press, London, UK, 2005.
- [14] A. Macchi, S. Veghini, T.V. Liseykina and F. Pegoraro. Radiation Pressure Acceleration of Ultrathin Foils. *New Journal of Physics*, 12(4):045013, 2010.
- [15] C. Thaury, F. Quere, J.-P. Geindre, A. Levy, T. Ceccotti, P. Monot, M. Bougeard, F. Reau, P. d'Oliveira, P. Audebert, R. Marjoribanks and Ph. Martin. Plasma mirrors for ultrahigh-intensity optics. *Nature Physics* 3(6):424-429, 2007.
- [16] A. Levy, T. Ceccotti, P. D'Oliveira, F. Reau, M. Perdrix, F. Quere, P. Monot, M. Bougeard, H. Lagadec, P. Martin, J.-P. Geindre, and P. Audebert. Double plasma mirror for ultrahigh temporal contrast ultraintense laser pulses. *Optics Letters* 32(3):310-312, 2007.
- [17] B. M. Hegelich, B. J. Albright, J. Cobble1, K. Flippo, S. Letzring, M. Paffett, H. Ruhl, J. Schreiber, R. K. Schulze and J. C. Fernández. Laser acceleration of quasi-monoenergetic MeV ion beams. *Nature*, 439(7075): 441-444, 2006.
- [18] A. P. L. Robinson, P. Gibbon, M. Zepf, S. Kar, R. G. Evans and C. Bellei. Relativistically correct hole-boring and ion acceleration by circularly polarized laser pulses. *Plasma Physics and Controlled Fusion*, 51(2):024004, 2009.
- [19] S. C. Wilks, A. B. Langdon, T. E. Cowan, M. Roth, M. Singh, S. Hatchett, M. H. Key, D. Pennington, A. MacKinnon, and R. A. Snavely. Energetic proton generation in ultra-intense laser-solid interactions. *Physics of Plasmas*, 8:542, 2001.
- [20] P Mora. Plasma expansion into vacuum. *Physical Review letters*, 90(18):185002, 2003
- [21] Laboratory for laser plasma, Shanghai Jiao Tong University website [online]. http://llp.sjtu.edu.cn/members/members_content.php?cid=171, accessed 20.06.2016.
- [22] T. Esirkepov, M. Borghesi, S. V. Bulanov, G. Mourou and T. Tajima. Highly Efficient Relativistic-Ion Generation in the Laser-Piston Regime. *Physical Review Letters*, 92(17):175003 (2004)
- [23] A. Macchi, F. Cattani, T. V. Liseykina and F. Cornolti. Laser Acceleration of Ion Bunches at the Front Surface of Overdense Plasmas. *Physical Review Letters*, 94(16), 165003 (2005).
- [24] Paul McKenna. *Laser-driven ion acceleration from ultrathin foil targets*. Available online at https://www.cockcroft.ac.uk/wp-content/uploads/2016/06/McKenna_Cockcroft-talk_w.pdf, accessed 20.06.2017.
- [25] D. Margarone, J. Krása, L. Giuffrida, A. Picciotto, L. Torrioni, T. Nowak, P. Musumeci, A. Velyhan, J. Prokúpek, L. Lásková, T. Mocek, J. Ullschmied, and B. Rus. Full characterization of laser-accelerated ion beams using Faraday cup, silicon carbide, and single-crystal diamond detectors. *Journal of Applied Physics*, 109(10): 103302, 2011.

- [26] G. Bertuccio, D. Puglisi, L. Torrisci and C. Lanzieri. Silicon carbide detector for laser-generated plasma radiation. *Applied Surface Science*, 272:128– 131, 2013.
- [27] G. Milluzzo. Diagnostics and dosimetry solutions for laser-driven ion beams: Preliminary results. Available online at <https://agenda.infn.it/getFile.py/access?contribId=239&sessionId=4&resId=0&materialId=slides&confId=8146>, accessed 21.06.2017.
- [28] M. Marinelli, E. Milani, G. Prestopino, C. Verona, G. Verona-Rinati, M. Cutroneo, L. Torrisci, D. Margarone, A. Velyhan, J. Krása and E. Krousky. Analysis of laser-generated plasma ionizing radiation by synthetic single crystal diamond detectors. *Applied Surface Science* 272:104– 108, 2013.
- [29] F. Grepl. *Diagnostics for laser-accelerated ion beams: design and signal processing*. Master thesis, Czech Technical University in Prague, Czech Republic, 2016
- [30] M. De Napoli, F. Giacoppo, G. Raciti, E. Rapisarda. Dopant concentration dependence of the response of SiC Schottky diodes to light ions. *Nuclear Instruments and Methods in Physics Research A* 600(3):618–623, 2009.
- [31] L. Calcagno, P. Musumeci, M. Cutroneo, L. Torrisci, F. La Via, J. Ullschmied. 4 MeV ion beams generated by intense pulsed laser monitored by Silicon Carbide detectors. *Journal of Physics: Conference Series*, 508(1):012009, 2014.
- [32] Wikipedia. Semiconductor detectors [online]. https://en.wikipedia.org/wiki/Semiconductor_detector, accessed 15.06.17.
- [33] Markus Friedl. *Diamond Detectors for Ionizing Radiation*. PhD thesis, Austrian Academy of Sciences, Vienna, 1999.
- [34] Wikipedia. Charge amplifier [online]. https://en.wikipedia.org/wiki/Charge_amplifier, accessed 22.06.2017.
- [35] Dirk Meier. *Cvd diamond sensors for particle detection and tracking*. Dissertation thesis, CERN, Geneva, 2009.
- [36] A. Alejo, D. Gwynne, D. Doria, H. Ahmed, D.C. Carroll, R.J. Clarke, D. Neely, G.G. Scott, M. Borghesi and S. Kar. Recent developments in the Thomson Parabola Spectrometer diagnostic for laser-driven multi-species ion sources. *Journal of Instrumentation*, 11(10):C10005, 2016.
- [37] A. Alejo S. Kar, H. Ahmed, A.G. Krygier, D. Doria, R. Clarke, J. Fernandez, R.R. Freeman, J. Fuchs, A. Green, J.S. Green, D. Jung, A. Kleinschmidt, C.L.S. Lewis, J.T. Morrison, Z. Najmudin, H. Nakamura, G. Nersisyan, P. Norreys, M. Notley, M. Oliver, M. Roth, J.A. Ruiz, L. Vassura, M. Zepf and M. Borghesi. Characterization of deuterium spectra from laser driven multi-species sources by employing differentially filtered image plate detectors in thomson spectrometers. *Review of Scientific Instruments*, 85(9):093303, 2014.
- [38] Jan Prokůpek, *Diagnostic Systems for Laser-Accelerated Ion Beams*, Master thesis, Czech Technical University in Prague, Czech Republic, 2012.

- [39] Wikipedia. J.J. Thomson [online]. https://en.wikipedia.org/wiki/J._J._Thomson, accessed 20.06.2017.
- [40] D. Jung R. Hörlein, D. C. Gautier, S. Letzring, D. Kiefer, K. Allinger, B. J. Albright, R. Shah, S. Palaniyappan, L. Yin, J. C. Fernández, D. Habs, and B. M. Hegelich. A novel high resolution ion wide angle spectrometer, *Review of Scientific Instruments*, 82(4):043301, 2011.
- [41] D. Kirby, *Radiation dosimetry of conventional and laser-Driven particle beams*, PhD thesis, The University of Birmingham, UK, 2011.
- [42] GafCromic films [online]. <http://www.gafchromic.com/> accessed 20.05.2017.
- [43] G. Milluzzo, V.Scuderi, A.G. Amico, G.A.P. Cirrone, G.Cuttone, M. De Napoli, J.Dostal, G. Larosa, R. Leanza, D. Margarone, G. Petringa, J. Pipek, F.Romano, F.Schillaci and A. Velyhan. TOF technique for laser-driven proton beam diagnostics for the ELIMED beamline. *Journal of Instrumentation*, 12(03):C03044, 2017.
- [44] Wikipedia. Return loss [online]. https://en.wikipedia.org/wiki/Return_loss, accessed 27.06.2017.
- [45] O. Klimo, J. Psikal, J. Limpouch, J. Proška, F. Novotny, T. Ceccotti, V. Floquet and S. Kawata. Short pulse laser interaction with micro-structured targets: simulations of laser absorption and ion acceleration. *New Journal of Physics*,13(5), 053028, 2011.
- [46] D. Margarone, O. Klimo, I. J. Kim, J. Prokůpek, J. Limpouch, T. M. Jeong, T. Mocek, J. Pšikal, H. T. Kim, J. Proška, K. H Nam, L. Štolcová, I. W. Choi, S. K. Lee, J. H. Sung, T. J. Yu and G. Korn. Laser-Driven Proton Acceleration Enhancement by Nanostructured Foils. *Physical review letters*, 109(23):234801, 2012.
- [47] L. Giuffrida, K. Svensson, J. Psikal, D. Margarone, P. Lutoslawski, V. Scuderi,d, G. Milluzzo, J. Kaufman, T. Wiste, M. Dalui, H. Ekerfelt, I. Gallardo Gonzalez, O. Lundh, A. Persson, A. Picciotto, M. Crivellari, A. Bagolini, P. Bellutti, J. Magnusson, A. Gonoskov, L. Klimsa, J. Kopecek, T. Lastovicka, G.A.P. Cirrone, C.-G. Wahlström and G. Korn. Nano and micro structured targets to modulate the spatial profile of laser driven proton beams, *Journal of Instrumentation*, 12(03):C03040, 2017.
- [48] L. Stolcova, J. Proška, F. Novotny, M. Prochazka and I. Richter. Periodic arrays of metal nanobowls as SERS-active substrates. *From Conference Proceedings Nanoccon. Brno: TANGER*, 737-741, 2011.
- [49] V. Floquet, O. Klimo, J. Psikal, A. Velyhan, J. Limpouch, J. Proška, F. Novotny, L. Stolcova, A. Macchi, A. Sgattoni, L. Vassura, L. Labate, F. Baffigi, L. A. Gizzi, Ph. Martin, and T. Ceccotti. Micro-sphere layered targets efficiency in laser driven proton acceleration. *Journal of Applied Physics*, 114(8):083305, 2013.

- [50] V. S. Belyaev, A. P. Matafonov, V. I. Vinogradov, V. Krainov, P. Lisitsa, V. S. Roussetski, A. S. Ignatyev, G. N. Andrianov. Observation of Neutronless Fusion Reactions in Picosecond Laser Plasmas. *Physical Review E*, 72(2):026406, 2015.
- [51] C. Labaune, S. Depierreux, C. Goyon, G. Loisel, V. Yahia and J. Rafelski. Fusion Reactions Initiated by Laser- Accelerated Particle Beams in a Laser-Produced Plasma. *Nature communications*, 4:2506, 2013.
- [52] A. Picciotto, D. Margarone, A. Velyhan, P. Bellutti, J. Krasa, A. Szydlowsky, G. Bertuccio, Y. Shi, A. Mangione, J. Prokupek, A. Malinowska, E. Krousky, J. Ullschmied, L. Laska, M. Kucharik, and G. Korn. Boron-Proton Nuclear-Fusion Enhancement Induced in Boron-Doped. Silicon Targets by Low-Contrast Pulsed Laser. *Physical Review X* , 4:031030, 2014.
- [53] D Margarone, A Picciotto, A Velyhan, J Krasa, M Kucharik, A Mangione, A Szydlowsky, A Malinowska, G Bertuccio, Y Shi, M Crivellari, J Ullschmied, P Bellutti and G Korn. Advanced scheme for high-yield laser driven nuclear reactions. *Plasma Phys. Control. Fusion*, 57:014030, 2015.
- [54] L. Giuffrida, D. Margarone, G. A. P. Cirrone, A. Picciotto, G. Cuttone, and G. Korn. Prompt gamma ray diagnostics and enhanced hadron-therapy using neutron-free nuclear reactions. *AIP Advances*, 6:105204, 2016.
- [55] H. Hora, G. H. Miley, M. Ghoranneviss, B. Malekynia, N. Azizi, and X. T. He. Fusion Energy without Radioactivity: Laser Ignition of Solid Hydrogen–Boron (11) Fuel. *Energy & Environmental Science*, 3(4):478-485, 2010.
- [56] C. Ohlandt, T. Cammash and K.G. Powell. A design study of p-11B gasdynamic mirror fusion propulsion system. *AIP Conference Proceedings*, Vol. 654, No. 1, pp. 490-496, 2003.